

Research paper

The technology of lunar regolith environment construction on Earth[☆]

Tao Zhang ^{a,b}, Chaoyue Chao ^a, Zhixiao Yao ^a, Kun Xu ^b, Wuxiang Zhang ^b, Xilun Ding ^{b,*}, Shuting Liu ^c, Zen Zhao ^d, Yinghe An ^{b,e}, Bing Wang ^a, Shuangfei Yu ^a, Bin Wang ^a, Haowen Chen ^a

^a School of Electro-mechanical Engineering, Guangdong University of Technology, Guangzhou, China

^b School of Mechanical Engineering and Automation, Beihang University, Beijing, China

^c Beijing Institute of Space Long March Vehicle, China Academy of Launch Vehicle Technology, Beijing, China

^d Beijing Spacecrafts, China Academy of Space Technology, Beijing, China

^e Space Engineering Development Co., Ltd., China Aerospace Science and Industry Corporation, Beijing, China

ARTICLE INFO

ABSTRACT

Keywords:

Lunar regolith
Environment construction
Thermal-vacuum preparation
Lunar regolith simulant
Gas-heat transfer mechanism

Lunar regolith plays an extremely important role in the establishment of permanent human residence or robotic industries on the Moon. Lunar regolith environment construction may accelerate the progress of lunar engineering, biology, medicine, and agriculture for future colonization of the Moon. Although advances in investigating and simulating lunar regolith have achieved unprecedented progress, producing simulated lunar regolith environment on Earth with adequate fidelity remains challenging. Inspired by traditional Chinese tofu making process, we proposed a comprehensive methodology to construct lunar regolith environment on Earth, and developed theoretical models to illustrate gas and heat transfer behavior in this particulate and porous material. Our study, proven to be effective, reveals a complex but generic gas and heat transfer mechanism in granular lunar regolith simulant, and can be readily applied to construct experimental regolith environments for lunar scientific research.

1. Introduction

Lunar exploration is an extremely challenging, innovative, and driving activity in the high-tech field of the world today, which has a great and far-reaching significance to the sustainable development of politics, economy, and culture of human society [3–5]. Recent research of lunar resource exploitation gained popularity among scientists and engineers worldwide because establishing permanent bases or settlements gradually becomes feasible as space technology advances [6–8]. Lunar regolith is a particulate and porous material covering lunar surface [9] and has probably the greatest application potential in supporting lunar habitation (Fig. 1)—including the fundamental building materials for civil engineering, the energy resources for space travel, the mineral resources for lunar robotic industry, the raw materials for lunar agriculture, and the chemical elements for lunar medicine because it is probably the only unlimited resource on the Moon, and is poised to advance the fields of space exploration, interstellar colonization, and planetary science [10–13]. To validate some key technologies for lunar habitation pre-research on Earth, the most crucial and generic techniques are lunar regolith simulant (LRS) fabrication and thermal-vacuum regolith environment construction to imitate lunar regolith for engineering application or scientific research [2,14,15].

Lunar surface is surrounded by extremely high vacuum (about 10^{-12} Pa), resulting in large temperature diurnal variation for no atmosphere to preserve heat [16]. In a lunar day, lunar surface has a large temperature variation ranging from -180 to 130 °C, but the regolith temperature below 300 mm is approximate -20 °C [17,18]. Except in polar regions and some permanently shadowed craters, lunar regolith is also anhydrous. The forming condition and ambient environment of lunar regolith contrast fundamentally to that of terrestrial regolith, lacking the effect of water flow, wind/oxygen erosion, and biological activities, and resulting in dramatically different mechanical and thermophysical characteristics [19,20]. The process is largely mechanical weathering in which particles are ground to finer and finer size over time, leading the particles to show the characteristics of obvious brittleness, porosity and multi-crack. These factors make lunar regolith a kind of granular, dry, and porous material with small particle size, irregular adsorption area, high gas solubility, and extremely large surface area-to-volume ratio. On Earth, gas fills in interparticle voids and particle internal pores of LRS, and plays a significant role in heat transfer [21,22]. That usually leads to huge outgassing rate during pump down and extremely low thermal conductivity in vacuum because heat transfer in LRS is mainly through solid conduction and

[☆] Beihang University and Guangdong University of Technology contributed equally in this work.

* Corresponding author.

E-mail address: xlding@buaa.edu.cn (X. Ding).

Nomenclature	
C_{gas}	Coefficient of gas convection in LRS (lunar regolith simulant) heat transfer, 2.03×10^{-22} [1]
C_{gs}	Coupling coefficient between solid conduction and gas convection, 6.0 by fitting
C_{rad}	Radiation coefficient in LRS heat transfer, 1.47 [2]
D	Gas diffusion coefficient inside LRS, m^2/s
E	Young's modulus, 78 GPa for typical basalt rock [2]
N_{Pr}	Prandtl number of air, 0.71 [1]
P	Gas pressure, Pa
Q_c	Outgassing and leaking of the chamber without LRS, Pa L/s
Q_r	Outgassing of LRS, Pa L/s
R	Radius of regolith container, m
R_p	Equivalent radius of LRS particles simplified as spheres, m
S	Surface area of compacted LRS, 3.6 m^2
S_e	Nominal pumping speed, L/s
T	Temperature, K
V	Volume of vacuum chamber, 4.3 m^3
ϵ	Thermal emissivity of LRS particles, 1.0 by assumption
κ	Surface energy representing the degree of adhesive force, 0.032 J/m^2 [2]
ϕ	Porosity of LRS, no unit
ρ	Bulk density of LRS, kg/m^3
ρ_{solid}	Density of the solid material to fabricate LRS, $2900 \text{ kg}/\text{m}^3$ for typical basalt rock [2]
σ	Mean diameter of air molecules, $0.33 \times 10^{-9} \text{ m}$
σ_{SB}	Stefan–Boltzmann constant, $5.67 \times 10^{-8} \text{ W}/(\text{m}^2 \cdot \text{K}^4)$
φ	Gas concentration inside LRS, mol/m^3
ξ	Thermal resistance coefficient between regolith particles for microscopic roughness, no unit
ζ	Specific heat ratio of air in room condition, 1.4
g_i	Function relates to conduction, convection, and radiation, no unit
k_{air}	Thermal conductivity of air, $\text{W}/(\text{m} \cdot \text{K})$
k_{basalt}	Thermal conductivity of typical basalt rock, $\text{W}/(\text{m} \cdot \text{K})$
k_{eq}	Equivalent thermal conductivity of LRS, $\text{W}/(\text{m} \cdot \text{K})$
k_{gas}	Heat transfer term by gas convection, $\text{W}/(\text{m} \cdot \text{K})$
k_{rad}	Heat transfer term by radiation, $\text{W}/(\text{m} \cdot \text{K})$
k_{sg}	Heat transfer coupling term by convection and conduction, $\text{W}/(\text{m} \cdot \text{K})$
k_{solid}	Heat transfer term by solid conduction, $\text{W}/(\text{m} \cdot \text{K})$
r_c	Radius of contact area between two spherical regolith particles, m
t	Time, s
v	Poisson's ratio, 0.25 for typical basalt rock [2]

and study [19,20,25], and space environment simulation has achieved remarkable advancement in the past several decades, they typically create space environments without granular regolith materials or with frozen regolith [14,26,27]. Conventional methods cannot simulate these equivalences simultaneously, particularly the thermophysical equivalence because the ultra-high vacuum of lunar regolith is almost impossible to achieve on Earth. To date, the methods to construct lunar regolith environment (LRE) remain limited and there still does not exist an instructively generic methodology, which has led us to question what makes LRE simulation difficult, and whether there exist theoretical models that can be generalized and applied to instruct LRE simulation with different conditions.

On the background of constructing a thermal vacuum lunar regolith environment for subsurface drilling test in Chinese Chang'E 5 mission, this work proposed a comprehensive methodology for LRS manufacture and environment simulation. The remainder of this work is organized as follows: Section 2 presents the schematic route for LRE construction; Section 3 introduces LRS fabrication method; Section 4 illustrates the design and development of a LRE simulator; Gas and heat transfer mechanism in particulate LRS is revealed in Section 5; Section 6 shows the application in Chinese Chang'E 5 mission; Section 7 discusses the limitation and application prospect of this method, and Section 8 concludes this work.

2. LRE construction methodology

Because lunar regolith is extremely rare and precious, current ground tests for engineering application or scientific research usually rely on LRS, which is the Earth substitute of lunar regolith for terrestrial application, such as the famous JSC-1 simulant (USA) and MKS-1 simulant (Japan) [2,28]. To construct similar regolith environment on Earth, three qualifications must be strictly satisfied:

- (1) *Mineral and chemical ingredients equivalence*: The main mineral and chemical ingredients should be similar, such as chemical element and mineral composition, which are usually satisfied during raw material collection. This is also the fundamental equivalence which determines the validity of lunar application tests in simulated terrestrial environment.
- (2) *Mechanical property equivalence*: The main mechanical characteristics should be similar, such as bulk density, porosity, particle size distribution, and inner fraction angle. It is mainly realized in fabricating LRS, and the most important principle is to pulverize the material to particles, dry the particles, mix the particles with desired size distribution, and compact it to desired density.
- (3) *Thermophysical property equivalence*: The critical thermophysical characteristics should be similar, such as thermal conductivity, specific heat, and thermal diffusivity. It is implemented in the

radiation inside and between regolith particles [23]. Large outgassing rate makes LRS difficult to pump, and low thermal conductivity makes it difficult to refrigerate in vacuum. Besides, if LRS is highly compacted, the inside gas molecules will be more difficult to desorb and diffuse, which may cause simulant disruptions, such as wave eruption, localized/surface boil and spout, leading to a decrease in bulk density, thereby reducing cohesion force, shear performance, and so on [15]. Freezing irrigated LRS is an efficient approach to achieve high vacuum, but this loses thermophysical equivalence [24]. To date, there is no precedent method to construct LRS with high density and compactness in vacuum environment.

Although the mechanical and thermophysical characteristics of surface lunar regolith have been well understood in previous exploration

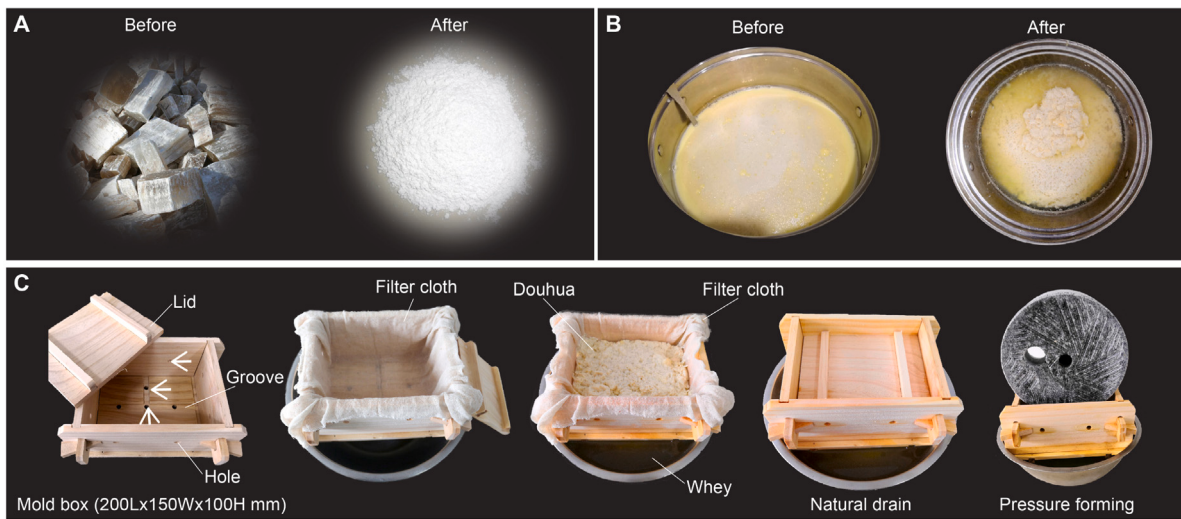


Fig. 1. Traditional Chinese tofu making process. (A) Coagulant. Natural gypsum crystal (left) was burned and then pulverized to powder (right) for soybean protein solidification. The best additive mass ratio of coagulant to dry soybeans is in the range of 2%~3%. (B) Douhua. Boiled soybean milk (left) was coagulated into douhua (right). (C) Tofu pressure forming art. Pine made mold box for tofu pressure forming (left to right): mold box, mold box lined with filter cloth, douhua wrapped up in filter cloth, natural drain, and pressure forming. The mold box has grooves or holes on side and bottom faces. The fine filter cloth contained thermally denatured soybean protein for initial whey draining, and then a heavy mass was loaded to accelerate tofu-whey separation for final forming.

later thermal-vacuum simulation, and the most important principle is to evacuate compacted LRS to desired vacuum and to heat/refrigerate it to desired temperature.

To achieve these equivalences, the core goal is to fabricate LRS and then to simulate a thermal-vacuum regolith environment.

2.1. Traditional Chinese tofu making process

As one consumable and delicious food, tofu, also known as bean curd, originated from ancient China, has graced Chinese tables for over 2000 years [29]. In the long history of evolution, the Chinese people formed mature production process for different kinds of tofu, however, the main production procedures remain the same (Fig. 1), including :

- (1) *Soybean grinding*: Soaked soybeans were gradually and finely ground by a traditional Chinese stone mill. Soybean protein membrane was pulverized by the scissoring force generated by the relative movement of stone teeth.
- (2) *Soybean milk/residue separation*: Then, we boiled the pulverized soybeans to dissolve protein in water as much as possible, and poured the heated mixture into a fine-mesh cloth bag for soybean milk/residue separation. The cloth-bag was manually squeezed to drain raw soybean milk.
- (3) *Raw milk boiling*: The raw milk was boiled for 3 min to make thermally denatured and then solidified soybean protein, and was naturally cooled down to 88~90 °C. Fifteen grams of calcined gypsum ($\text{CaSO}_4 \cdot 2\text{H}_2\text{O}$) was added into the milk, and soybean protein coagulated into douhua after 5 min.
- (4) *Tofu pressure forming*: The coagulated douhua was stirred into small pieces to facilitate tofu/whey separation, and then poured into a filter cloth lined mold box (pine-made, with grooves or holes on side and bottom faces). Finally, a heavy object was loaded on the lid of the mold box to drain whey for 40 min.

2.2. Schematic methodology

Generally, two steps are critical in tofu making: (i) soybean milk preparation, and (ii) tofu/whey separation. Taking inspiration from this process, we proposed a comprehensive methodology for LRE simulation, as shown in Fig. 2. In this process, LRS fabrication is inspired

by soybean milk preparation, while evacuation is strongly inspired by tofu/whey separation.

Raw material for LRS fabrication was collected from volcanic scoria, which had been proven to have similar ingredients with lunar regolith (Fig. 2A). To pulverize the raw material into small particles, a hydraulic Ramon grinder was used for smashing (Fig. 2B). Then, the pulverized material was screened into different-size particles by a vibration separator (Fig. 2C). The dehydrated and dried particles (Fig. 2D) had been generally airtight stored before it was utilized for engineering or scientific application. To fabricate LRS with different geologic characteristics, dried particles were stirred and mixed according to desired size distribution (Fig. 2E). The mixed LRS was mechanically compacted to desired bulk density by vibration method (Fig. 2F). Before thermal environment simulation, LRS was pumped down to vacuum (≤ 10 Pa) in advance to restrain water freezing and weaken heat transfer (Fig. 2G). To deal with LRS material with huge outgassing, the evacuation process was highly inspired by tofu-whey separation, in which holes were machined on the side/bottom of the container to shorten airflow path and facilitate outgassing. It is worth noting that the fine filter cloth is a critical tool in tofu making, which enables the whey to drain from the bottom and side of mold box. During the evacuation process, gas was be pumped away through the nearest path to LRS surface, just like water was drained from the side and bottom of mold box in tofu making. This is extremely important to evacuate materials like LRS with a huge outgassing rate. Lunar surface has a negative thermal gradient in depth during lunar daytime and a positive gradient during nighttime. Here only daytime thermal gradient is considered as most planetary operations are conducted during lunar daytime. As gas convection disappears and radiative transfer is low-efficient in low temperature, therefore conductive heat transfer is the most effective way for refrigeration in vacuum. To establish stable temperature gradient with depth as in case of lunar regolith daytime condition, the strategy is heating the top and cooling the bottom of the regolith container. In engineering implementation, the surface high temperature was realized by radiation, while the subsurface layer was refrigerated by vertically distributed coppers inside LRS and circularly winded coppers outside the regolith container (Fig. 2H). The temperature gradient along depth and radius was measured with thin temperature strings (1-mm diameter PT100 distributed along a cable) embedded inside LRS, as published in our previous work [30].

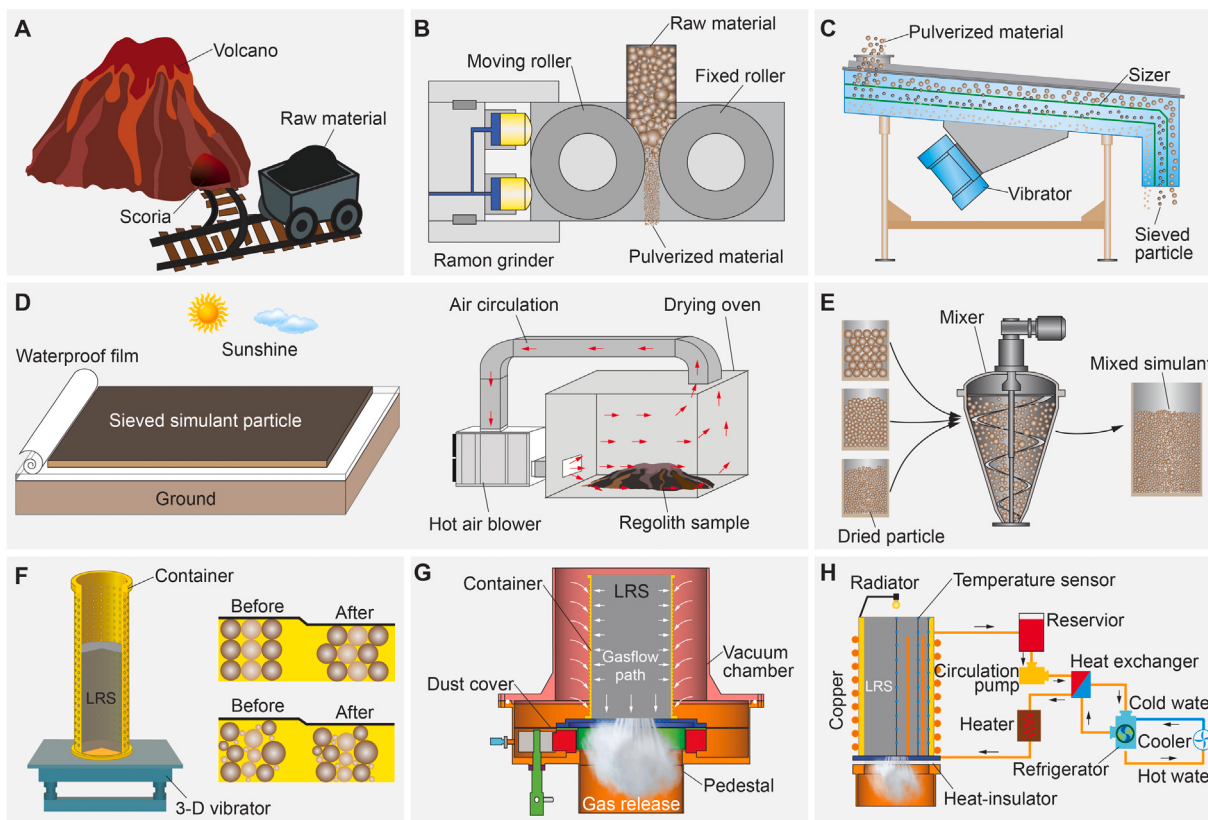


Fig. 2. Schematic illustration of the simulation methodology for LRE. (A) Raw material collection. Volcanic scoria is considered as the best raw material candidate for LRS fabrication. (B) Mechanical fragmentation. Raw material was crushed into particles with small sizes by a Ramon grinder. (C) Particle screening. Crushed material was separated into different piles according to sizes. (D) Dehydration and drying. Sieved particles were dehydrated by sunlight (left) first, and then dried by a thermal air circulation oven (right). (E) Stirring and mixing. Particles with different sizes were mixed according to desired size distribution for simulating lunar regolith at different sites. (F) Vibratory compaction. Mixed simulant was vibrated to desired bulk density by a 3-dimensional vibrator. (G) Evacuation inspired by tofu making. Gas inside LRS released from the nearest path to surface and was pumped away from the container bottom, just like the whey draining process in tofu forming. (H) Temperature gradient simulation. The top 300-mm LRS was heated by radiation, while the deeper layer was refrigerated by conductive heat transfer.

3. LRS fabrication

According to the research on the regolith samples returned in previous Luna and Apollo missions, the compositions and ingredients of lunar regolith are extremely complicated and vary with sampling locations [31–33]. However, the main aspects remain in certain range, such as the main chemical elements are O, Si, Al, Ca, Mg, Fe, and Ti, and almost all samples are mainly made up of certain rocks and minerals: mineral debris, original crystalline rock fragment, breccia or glass debris, and meteorite debris [19,34].

In principle, to simulate lunar regolith in specific locations, we should not only take into account the integrated analysis of lunar regolith formation history, ambient environment, moon surface topography, chemical/mineral composition, particle size and compaction status, but also consider the influence on the properties caused by low gravity, high vacuum, and large thermal fluctuation. Lunar surface regolith contains various materials, which vary with altitudes, longitudes, latitudes, landforms, or even depths in the same site. There are a variety of parameters indicating the characteristics of lunar regolith, however, taking all parameters into consideration simultaneously is unpractical in ground operation. Therefore, the reproduction becomes difficult because of the diversity and unevenness of lunar regolith. Based on these considerations, the conventional way is to simulate the parameters that may greatly influence the experimental results, from the viewpoints of reproducibility and controllability. We classified them into controlling index and measuring index, and then divided the indices into three levels according to difficulty or importance (Fig. 3A). The controlling indices should be actively satisfied during fabrication,

while the measuring indices only need to be passively detected afterwards. For property equivalence, the most important thing is to collect raw material (Fig. 3B to E) to achieve a better simulation not only for the mechanical properties of lunar regolith at the macro level, but also for the chemical/mineral properties at the micro level. We collected basaltic volcanic scoria from Huinan area of Jingyu, Jilin province, China, which has similar chemical and mineral compositions with low-Ti regolith in lunar mare. The LRS in our experiments was produced for ground tests of the third stage of China's Chang'E lunar exploration project. The sieved regolith particles with different sizes are presented in Fig. 3F to M.

3.1. LRS drying and compaction

3.1.1. LRS drying

Drying is one of the key procedures in LRS fabrication, including drying by sunlight and baking by oven.

- (1) *Natural drying by sunlight:* After being pulverized by Ramon grinder, regolith particles were sieved and laid on ground for natural dehydration by sunshine. A thick waterproof plastic film (polyvinyl chloride) was laid below the LRS to prevent it from being contaminated by ground regolith particles and to prevent the upward transmission of water vapor. LRS was uniformly paved on the film with a thickness of 20 mm, then another plastic film covered its surface, acting as moisture-proof tarp at nighttime and water-proof tarp in raining days. The upper plastic film was uncovered to expose LRS to sunshine except in cloudy and rainy daytime, which was the preliminary dehydration.

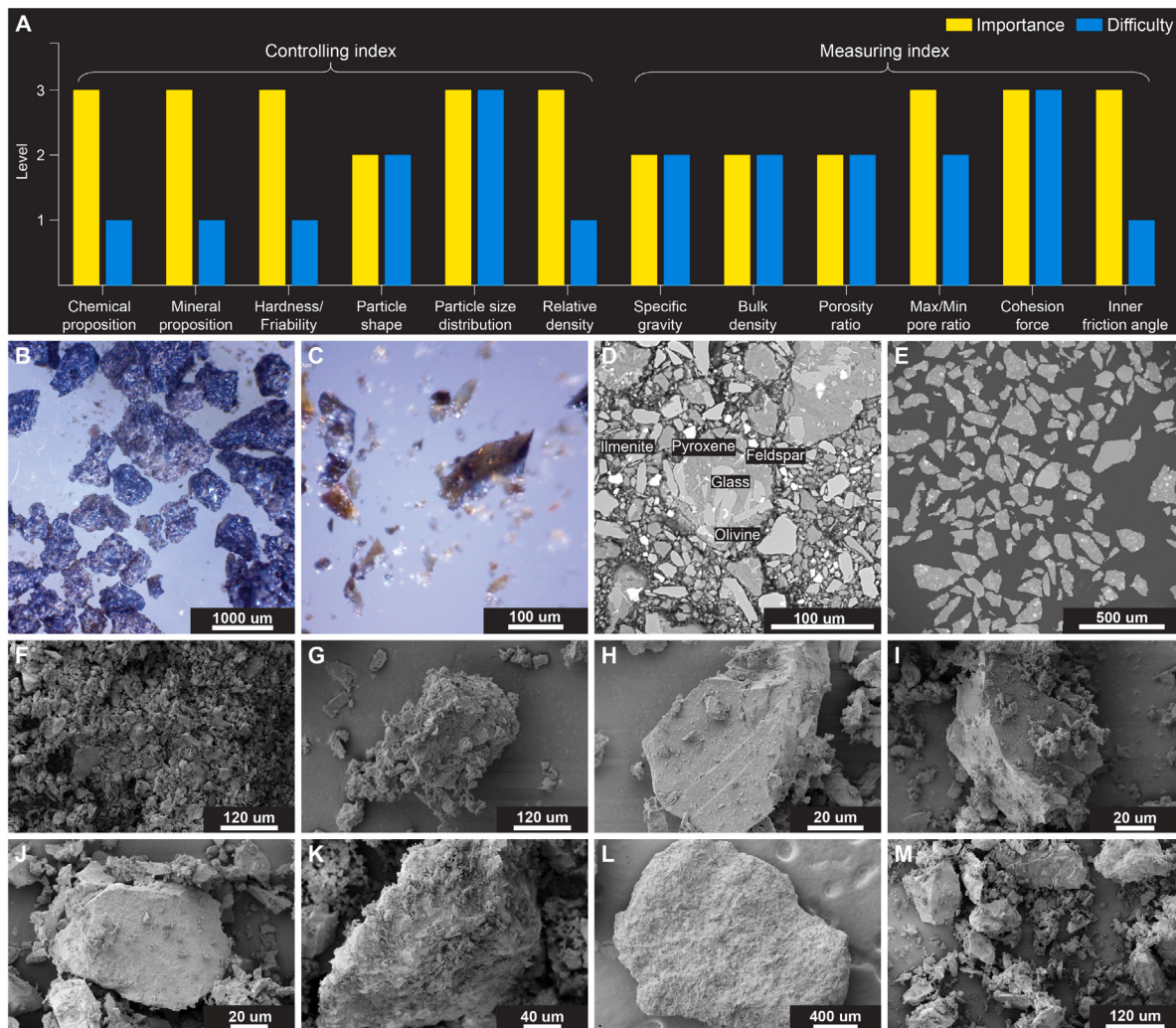


Fig. 3. LRS fabrication. (A) Classification of characteristic indices for LRS. Importance levels 1~3 mean less, middle, and very important. Difficulty levels 1~3 mean easy, moderate, and difficult to reach. These indices are divided according to the methodology utilized in terrestrial regolith study. (B and C) Micro-image of raw material–volcanic scoria particle magnified 60 times (B) and 540 times (C), taken by a digital microscope (GE-5), showing obvious particle angle, irregular particle shape, and considerable glass. (D) SEM image of raw material: lightness represents the molecular weight of different minerals. (E) Typical particle shapes of raw material. (F to M) Microscope images of LRS particle with different sizes, photographed by a scanning electron microscope (SEM, ZEISS EVO 18). (F) 0~10 μm . (G) 10~25 μm . (H) 25~50 μm . (I) 50~75 μm . (J) 75~100 μm . (K) 100~1000 μm . (L) 1000~2000 μm . (M) Mixture of particles with different sizes.

(2) *Laboratory drying by baking:* In room environment, LRS was baked by a heat air circulation oven (WGL 230B) with a temperature of 120 °C (a little higher than the boiling point of water, a balance in baking efficiency and content non-modifiability) for 16 h. For each 2 h, LRS sample was weighed with an accuracy of 0.001 g. Until there was no change in weight, the final water content was controlled to be less than 0.1%.

3.1.2. LRS compaction

In engineering application and scientific research, LRS with different bulk densities is usually necessary to simulate different experimental conditions. We proposed a method to implement this goal by 3-dimensional vibration. The two critical steps are as follows:

(1) *Regolith particle mixing:* To simulate lunar mare regolith, we mixed the sieved and dried regolith particles with this ratio: 13.51% for particle size smaller than 10 μm , 11.99% for particle size in the range of 10~25 μm , 12.83% for 25~50 μm , 8.24% for 50~75 μm , 5.53% for 75~100 μm , 14.2% for 100~250 μm , 10.2% for 250~500 μm , 8.5% for 500~1000 μm , and 15% for particle size larger than 1000 μm . These regolith particles were mixed evenly through a spiral stirrer (None-standard, custom-made).

(2) *Layer-by-layer compaction:* We weighed a certain mass Δm_i of mixed LRS and then filled it into the container, in which $i = 1, 2, 3, \dots, N$ means the filling time. In practical operation, we filled the container in four times with the same mass of 93.76 kg, which means the final mass was near 375 kg. Then the container was covered by cloth to restrain dust rising and a 3-dimensional vibrator (None-standard, custom-made) was used for LRS compaction, which has a frequency of 30 Hz generated by vibration motors in three directions. The vibration started in the vertical direction first, and then in the horizontal plane. We measured the height h of the compacted regolith inside the container after every 5-min vibration, and calculated the bulk density according to:

$$\rho_{\text{bulk}} = \sum_{i=1}^n m_i / \left(\frac{\pi}{4} d^2 h \right) \quad (1)$$

where d is the inner diameter of the container. In principle, different bulk densities could be reached through controlling vibrating time. For our experimental purpose to construct LRE in extreme conditions, we continued the vibration until the desired average bulk density of 1910 kg/m³ was reached.

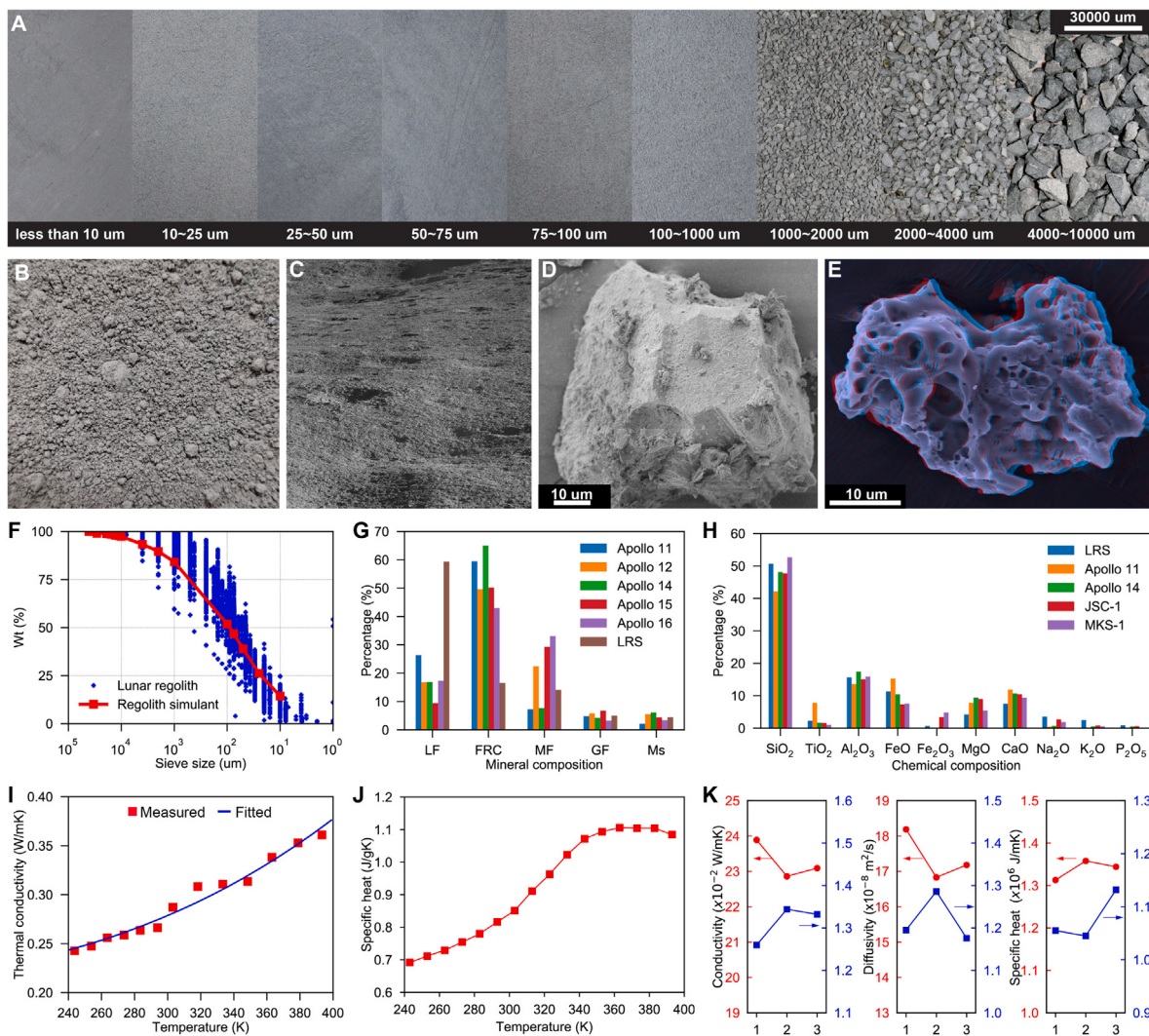


Fig. 4. Characteristic equivalence of the fabricated LRS. (A) LRS ingredients with different particle sizes. (B) Fabricated LRS in loose condition. (C) Lunar surface regolith photographed by the lander of China's Chang'E 4 mission (Credit: China National Space Administration, CNSA). (D) Scanning electron microscope (SEM) image of LRS particle. (E) SEM image of lunar dust (Credit: Lehigh University). (F) Size distribution comparison between our LRS and lunar regolith. The number of blue points is approximate 4000, which were summarized according to the compilation by Graf [35] from nearly 350 samples returned in the six landing missions in American Apollo project. (G) Mineral composition comparison between our LRS and lunar regolith. The mineral compositions of lunar regolith were summarized according to Ref. [36]. LF, FRC, MF, GF, and Ms mean lithic fragments, fused regolith components, mineral fragments, glass fragments, and miscellaneous, respectively. (H) Chemical composition comparison between our LRS and lunar regolith (simulant) [36,37]. The sample was dried first, and the powder with size less than 0.25 mm was screened for X fluorescence spectrometer test and X-ray photoelectron spectroscopy to detect its chemical elements. (I) Thermal conductivity of our LRS versus temperature at NAP. The measured sample was manually compacted by testers to a bulk density of 1875 kg/m³. According to the most widely used Watson's equation [38], the fitted thermal conductivity curve can be expressed as: $k_{LRS} = 2.07 \times 10^{-1} + 2.67 \times 10^{-9} \cdot T^3$ (blue line). We only measured the values from 240 K to 400 K (with the standard transient hot-wire method) because lunar regolith temperature is almost in this range during lunar daytime. (J) Specific heat of our LRS versus temperature at NAP. We also manually compacted the samples to a bulk density of 2046 kg/m³. (K) Thermal property comparison of our LRS at NAP (red line) and 1-Pa vacuum (blue line), both at 293 K, including thermal conductivity, thermal diffusivity, and specific heat. Each parameter was repeatedly measured three times. (For interpretation of the references to colour in this figure legend, the reader is referred to the web version of this article.)

3.2. Property equivalence

The fabricated LRS, in loose state, is presented in Fig. 4A and B to make a visual contrast with lunar regolith (Fig. 4C). Because of Earth gravity, the stored LRS is much easier to agglomerate than lunar regolith in low gravitational environment. In Fig. 4D and E, we compared the microparticle shape of LRS with that of lunar regolith. Although these particles have a similar size, it is obvious that the lunar regolith particle is more porous, resulting in a much larger surface area-to-volume ratio, while the surface of newly fabricated LRS particle is much flatter. This is because lunar regolith particle was mechanically weathered by the unique lunar environment in the long time of evolution, resulting in its special porosity and frangibility, which is almost impossible to simulate on planet Earth in short time. In Fig. 4F to H, we compared the size distribution, and mineral/chemical compositions of

LRS with that of lunar regolith samples returned in Apollo project, and the most widely used regolith simulant JSC-1 and MKS-1, fabricated by USA and Japan, respectively. Once regolith particles with different sizes are screened, the size distribution controlling becomes easy. Our LRS, aiming to mimic lunar mare regolith, has an equivalent size distribution with samples returned in six Apollo missions. The mineral and chemical compositions are mainly determined in collecting raw material. The LRS has a similar mineral composition with regolith sample returned in Apollo 16 mission, and a close chemical composition with samples returned in Apollo 11/14 missions, also with JSC-1 and MKS-1 simulants. The thermal conductivity of compacted LRS is near 0.24 W/(m·K) at 240 K and 0.36 W/(m·K) at 390 K (Fig. 4I) at normal atmospheric pressure (NAP). Compared with 2.17 W/(m·K) of raw basalt at 240 K, the thermal conductivity is only near one-ninth, which means heat transfer is sharply weakened in particulate and porous LRS. However,

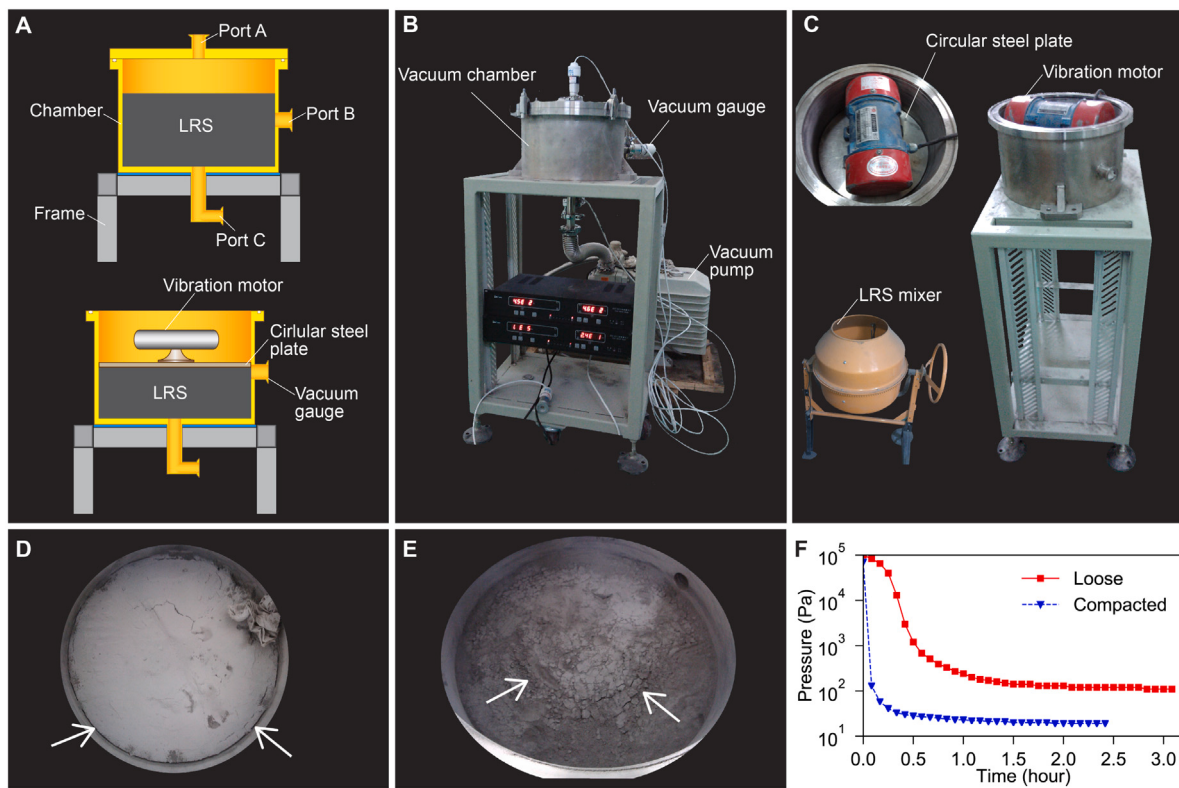


Fig. 5. Test-bed for pre-validation of LRS compaction and evacuation. (A) Schematic illustration of compaction and evacuation method for LRS. The vacuum chamber was made of 304 stainless-steel and electropolished to restrain outgassing. It has an inner diameter of 308 mm, and a height of 200 mm. Three ports locate at the top, side and bottom faces, respectively. Ports A and C are interfaces for vacuum pump connection, and port B is for vacuum gauge fixation. A vibration motor with a circular steel plate was used for LRS compaction. (B) The practical test-bed. (C) LRS compaction process. Inset: vibration motor inside vacuum chamber (top) and LRS stirring mixer (bottom). (D) Image after pumping from port C. It clearly shows that a gap was generated between chamber side face and LRS for gas flow, and sample compactness was maintained well. (E) Image after pumping from port A. Sample surface became loose and blocky, which means dust raised during pumping and scattered after pumping. (F) Comparison of pressure variation between loose and compacted LRSs. In both experiments, the chamber was pumped from port C by a rotary-vane pump with a speed of 19 L/s.

the specific heat at 300 K (Fig. 4J), 0.84 J/(g·K), is almost the same with that of basalt rock, as well as near with 0.75 J/(g·K) of lunar regolith sample returned in Apollo 11 mission [39]. We also measured the most important three thermal parameters, namely thermal conductivity, thermal diffusivity and specific heat, at both NAP and 1-Pa vacuum (Fig. 4K). The first two parameters are greatly weakened in vacuum, and the value is only 5% ~ 7% of that at NAP, while the specific heat almost remains the same, showing a same tendency with that of lunar regolith [20]. This can be explained that the thermal conductivity of gas, indicating heat transfer capability, is almost the same order with that of LRS particles at NAP, while its specific heat, indicating heat storage capability, is far lower. Therefore, the heat stored in the gas, existing in interparticle void, can be neglected, while the heat transferred by the gas is considerable.

4. Development of LRE simulator

Conventionally, there are two main methods for simulating extraterrestrial regolith environments: (i) natural method is to find a similar regolith environment on Earth [40], and (ii) man-made method is to construct a laboratory regolith environment manually [41]. The natural way is low cost and able to well simulate the complexity and variability of stratum, however, only certain parameters can be well satisfied, while the remaining parameters may be sharply different from extraterrestrial environment, such as gas pressure and water content. Although the man-made way is high cost and the simulated parameters are relatively fewer, however, its advantages are also obvious for every parameter is highly controllable, which does well in studying the influence of a single parameter.

4.1. Pre-validation experiment

To pre-validate our methodology of LRS compaction and evacuation, we developed a small test-bed first (Fig. 5). We pumped from the top or the bottom of the regolith container and compared the final states of LRS. The results show that the bottom-pump has a strong advantage in maintaining LRS compactness. We also compared the evacuation results of compacted LRS with that of loose LRS, which demonstrates that it is much easier to pump compacted LRS in the same experimental conditions. That is because less gas remains inside highly compacted LRS, resulting in a low outgassing rate. After this successful pre-validation, we established a comprehensive methodology to construct LRE for experiments, and the routine for conducting experiments is:

- (1) Experiment preparation is completed by manual work. Most of the work focuses on cleaning the inner surface of vacuum chamber with industrial pure alcohol. Pure acetone is not chosen because it does harm to human health.
- (2) LRS compaction is finished by a 3-D vibrator for desired bulk density. LRS is also stirred and mixed according to desired size distribution before compaction.
- (3) Evacuation is realized by the vacuum pump system. This is the most difficult step in the whole process. What is particularly noteworthy is that evacuation must be done before refrigeration, because the water in air would turn into ice and remain inside LRS if refrigeration is done in advance, changing water content and then heat transfer.

- (4) Refrigeration is applied by the cooling circulation system. This is the most time-consuming step because of low heat transfer efficiency in vacuum. We need to reasonably lay cold source for fast thermal field simulation.
- (5) Radiation is finished by the heating system. This is the easiest and fastest step in the whole process for the high efficiency of radiative heating.
- (6) Finally, we can carry out desired experiments in the simulated LRE.

4.2. Test-rig fabrication

4.2.1. Vacuum pump system

The designed vacuum chamber has three components: an upper chamber for containing objects to be tested, a lower chamber for LRE simulation, and a pedestal for vacuum-pumping. The chamber is made of 304 stainless-steel, with electropolished inner surface to restrain outgassing, and is evacuated by the specially designed three-stage vacuum pump system. The initial vacuum acquisition capability of the test-rig was designed to be: (i) 10^{-2} Pa within 24 h without LRS, and (ii) 10 Pa within 24 h with LRS. Considering the practical situation with abundant particulate and porous LRS, oil diffusion pump was chosen for its low demand in chamber cleanliness and high dust resisting performance. A diffusion pump (KT-630, 1.8×10^4 L/s at 6×10^2 Pa) was used for high vacuum-pumping. A rotary-vane pump (2X-15, 1.5×10^1 L/s at 1×10^5 Pa) maintained the fore-vacuum for the diffusion pump. Two rotary-vane pumps (2X-70, 7×10^1 L/s at 1×10^5 Pa) were used for auxiliary fore vacuum-pumping. A roots pump (ZJP-600, 6×10^2 L/s at 5×10^2 Pa) connected the rotary-vane pumps with the diffusion pump for evacuation acceleration. The vacuum pump system was equipped with a water circulation system (KCRH CH-120A) for cooling (20°C -water), and an air compressor (ZWB-110, 8×10^5 Pa) to provide pneumatic power for electromagnetic valve control. A water-cooling baffle (SDB-630) was installed between the inlet of the diffusion pump and the pedestal to reduce oil return from the diffusion pump.

4.2.2. LRS particle filtration

For dust protection and LRS density maintenance during pump down process, a special filtering architecture was designed. Three layers of stainless-steel screens were tightly placed on the inner surface of regolith container, whose mesh sizes were determined according to the size distribution of LRS particles. As the particles larger than 25 μm account for 74.5% in LRS, therefore, a 500-mesh screen (25 μm size) can prevent a majority of the particles. Combining with an 800-mesh screen (15 μm size), the screens can retain most of the particles. In addition, as LRS is blended with small-scale basalts and needs to be compacted by a 3D vibration device during preparation, the thin screens are easy to be cut by the sharp corners of basalts, hence screens with larger mesh size (1-mesh and 300-mesh) and thicker mesh wire are laid to the inner side of the 500-mesh screen. The filtering screens were designed as two semi-circular cylinders, which naturally opened by regolith pressure during vibration. A dustproof baffle surrounded the bottom of the regolith container to prevent slewing bearings and gears being contaminated by dust.

4.2.3. Heating and refrigeration

Three 200-W iodine-tungsten lamps (FSL 220V) were used for heating, which have a highest radiative temperature of 250°C . An oil cycle refrigerating machine (SUNDI-575 W, 7.5 kW) with continuous outlet temperature controlling ability provided coolant (silicone oil, KDOC-220) circulation. The designed heat exchange method is to wind copper coils on the exterior surface of regolith container and to arrange vertical pipes inside LRS, except the top 300 mm, for LRS refrigeration by conductive heat transfer. The machine refrigerated LRS by continuously circulating silicone oil with an outlet temperature of -55°C . The lowest temperature that the copper coil can withstand is -196°C . In order to increase the contact area between the coil and the container, spiral grooves were machined on the outer surface of the container.

4.3. Development and experiments

Based on the proposed methodology, we designed and developed a test-rig for LRE simulation (Fig. 6A to C). Taking inspiration from tofu making, gas inside compacted LRS can be more fluently released through holes on the side/bottom of the regolith container as outgassing path is highly shortened, and then pumped from its bottom (see pre-validation). Considering the huge outgassing of powdered LRS, a three-stage vacuum pump system was designed for evacuation (Fig. 6D). The thermal characteristics of simulated LRE are highly dependent on water content and ambient air pressure, however, the ultra-high vacuum of lunar regolith is almost impossible to achieve on Earth. Fortunately, previous researches show that the thermophysical characteristics of lunar regolith are essentially independent of ambient pressure when it is below 10 Pa [42,43]. That means, in ground simulation, a relatively low vacuum (less than 10 Pa) can effectively guarantee the thermophysical equivalence. Then, we set the target pressure to the range of 1~10 Pa. To prevent LRS particle leaking, multilayer fine stainless-steel meshes were employed based on the size distribution of LRS (Fig. 6E). In Fig. 6F, we demonstrate the method to embed sensors for distributed temperature and pressure measurements during the layer-by-layer compaction of LRS. Through this way, lunar rock simulant can be laid to desired location and sensors can measure the thermal field and inner pressure in real time. Fig. 6G shows that it only took 2.8 h to reach 9.48×10^{-2} Pa with empty chamber, while the pressure merely reached 1.13 Pa after 6.5 h when LRS was included, proving the huge outgassing rate of LRS. For temperature gradient simulation in vertical direction, a heating/refrigerating module was designed to heat/refrigerate and maintain the required surface/subsurface temperature of LRS during tests. High temperature simulation is implemented by using iodine-tungsten lamps as rapid heat source in vacuum, which located directly above the regolith container. Different from liquid nitrogen generally used for refrigeration, we adopted an oil cycle refrigerating machine as the cold source, which uses silicone oil as coolant. The results show that LRS deeper than 0.4 m reached the temperature lower than -23°C after 32 h, which is far enough to mimic lunar subsurface thermal condition (Fig. 6H). The surface temperature reached 85.5°C within 47.6 min for simulating sunlight heating during lunar daytime (Fig. 6I). The subsurface temperature decreased only 0.1°C in 24 min after 32-hour refrigeration, which is far stable enough for our 20-min drilling and sampling experiment.

5. Heat and gas transfer mechanism in LRS

5.1. Theoretical analysis

5.1.1. Gas transfer mechanism

Every solid material absorbs gas at NAP, and gas desorbs from material surface in vacuum, namely outgassing. Outgassing rate is defined as gas release quantity per unit time, and the magnitude depends on various factors, such as material nature, storage manner, surface treatment, or even manufacturing process. It has extremely important application for vacuum system design and fabrication, particularly for ultrahigh vacuum, because materials with large outgassing rate make it challenging to reach desired vacuum, even excellent sealing materials are utilized. Outgassing can be divided into two steps: (i) gas desorption from material surface, and (ii) gas diffusion inside material. Generally, desorption and diffusion are the main causes of outgassing, which are usually proportional to gas pressure difference. Compared with conventional metals, particulate and porous LRS has higher surface area-to-volume ratio and larger particle porosity to retain gas, resulting in a far large outgassing rate.

To estimate the outgassing rate of LRS during pump down, we conducted a controlled experiment: (i) pumping the vacuum chamber without LRS first to acquire the leaking and outgassing of the test-rig, and then (ii) pumping the vacuum chamber with LRS to acquire the

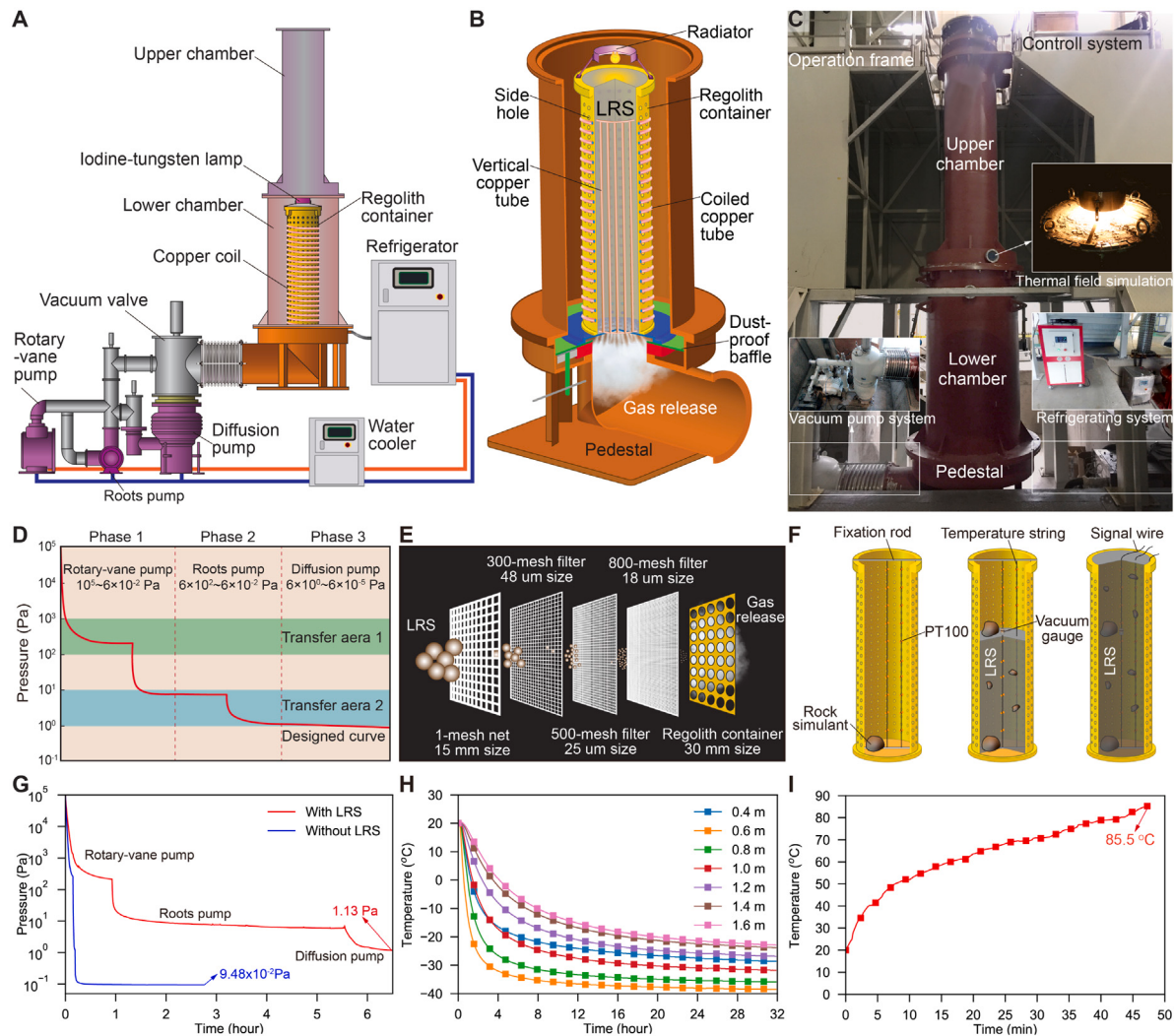


Fig. 6. Test-rig design, development and experimental validation. (A) Schematic illustration of the proposed test-rig, including a chamber, a vacuum pump system, and a refrigerating/heating system. The chamber is divided into two sub-chambers: the upper chamber provides space for systems to be tested and the lower chamber is for LRE simulation. (B) Three-quarter section view of the simulator inspired by tofu making. The regolith container has an inner diameter of 0.5 m and a height of 2.05 m, and holes with a diameter of 30 mm were machined on the container's side and bottom faces for outgassing. Copper tubes are coiled round and vertically laid inside the container, except the top 300 mm, for conductive heat exchange by coolant circulation. (C) Practical test-rig. The chamber has a height of 6.05 m. The lower/upper chamber has a diameter of 1.16/0.70 m. Chambers are sealed by compressing full-cycle O-rubber rings smeared with vacuum grease. Inset: vacuum pump system (left), thermal field simulation (right top), and refrigerating system (right bottom). (D) Schematic illustration of evacuation strategy. A three-stage vacuum pump system was designed to evacuate LRS material with huge outgassing. We defined two pump-transfer pressures: the first is 200 Pa from rotary-vane pump to roots pump, and the second is 6 Pa to diffusion pump. (E) Multilayer mesh filtration method. The screens are stainless-steel (1/300/500/800 mesh, from inside to outside). (F) LRS compaction and sensor arranging method. Platinum resistors (PT100) and rock simulant (basalt) fixation (left), vacuum gauge fixation (middle), and compacted LRS with defined regolith condition and sensor measurement (right). (G) Pressure versus time with (red line) and without (blue line) LRS. (H) Refrigerating temperature versus time (the temperature string was 50 mm from vertically distributed copper axis). (I) Heating temperature versus time (the sensor located in the center of LRS surface). (For interpretation of the references to colour in this figure legend, the reader is referred to the web version of this article.)

outgassing of LRS. We assume the test-rig has the same leaking and outgassing at the same pressure. The pump configuration is the same at the same chamber pressure to ensure the vacuum pump system has the same pumping speed. According to vacuum theory, when LRS is not included in the chamber, the evacuation equilibrium equation can be denoted as [44]:

$$V \frac{dP(t)}{dt} + S_e(P) P(t) = Q_c \quad (2)$$

In Eq. (2), Q_c is assumed to be constant for its value is far small compared with Q_r , and it can be measured by conducting static pressurization experiment to the vacuum chamber. Giving measured pressure variation with time, S_e in certain P can be obtained easily by:

$$S_e(P) = \frac{1}{P} \left(Q_c - V \frac{\Delta P}{\Delta t} \right) \quad (3)$$

When LRS is included, then Eq. (2) can be rewritten as:

$$V \frac{dP(t)}{dt} + S_e(P) P(t) = Q_c + Q_r(t) \quad (4)$$

For a given time t , then we have:

$$Q_r(t) = V \frac{\Delta P}{\Delta t} + S_e(P) P - Q_c \quad (5)$$

Then we can obtain the outgassing rate of LRS simply by dividing the surface area:

$$q_{gr}(t) = \frac{Q_r(t)}{A} \quad (6)$$

Previous researches show that the outgassing rate of material can be expressed as [44]:

$$q(t) = q_0 e^{-m \log t} \quad (7)$$

where q_0 and m are constants relating to its physicochemical characteristics. In our work, we roughly fitted the outgassing rate of LRS with the coefficients of $q_0 = 6.24 \times 10^3$ and $m = 1.20$ [23].

For theoretical analysis, the LRS can be viewed as a cylindrical body exposed to vacuum in the simulation chamber. The gas desorption of LRS surface is modeled as Eq. (7), while the internal gas diffusion needs to be depicted by Fick's second law:

$$\frac{\partial\varphi}{\partial t} = \nabla^2(D \cdot \varphi) \quad (8)$$

To simplify the case, we assume the compacted LRS to be an infinite cylinder. In cylindrical coordinate, Eq. (8) can be written as:

$$\frac{\partial\varphi}{\partial t} = \frac{1}{r} \left(\frac{\partial}{\partial r} \left(Dr \frac{\partial\varphi}{\partial r} \right) + \frac{\partial}{\partial \theta} \left(D \frac{1}{r} \frac{\partial\varphi}{\partial \theta} \right) + \frac{\partial}{\partial z} \left(Dr \frac{\partial\varphi}{\partial z} \right) \right) \quad (9)$$

Given that LRS is homogeneous in all directions for gas diffusion, then we have $\frac{\partial\varphi}{\partial \theta} = \frac{\partial\varphi}{\partial z} = 0$ and Eq. (9) can be simplified to:

$$\frac{\partial\varphi}{\partial t} = \frac{1}{r} \frac{\partial}{\partial r} \left(Dr \frac{\partial\varphi}{\partial r} \right) \quad (10)$$

We take the ideal condition into consideration, in which the chamber pressure changes into absolute vacuum when the pump system starts to work, then the boundary conditions can be given as:

$$\begin{cases} \varphi = \varphi_0 \text{ in } 0 < r < R \text{ when } t = 0 \\ \varphi = 0 \text{ in } r = R \text{ when } t > 0 \end{cases} \quad (11)$$

Following essentially the method of separation of variables, we have a solution for constant D provided u is a function of r only:

$$\varphi(x, t) = u \exp(-Dx^2 t) \quad (12)$$

Substitute Eq. (12) into Eq. (10), then we can get:

$$\frac{d^2u}{dr^2} + \frac{1}{r} \frac{du}{dr} + \alpha^2 u = 0 \quad (13)$$

Eq. (13) is a typical Bessel's equation of order zero, and its solution may be obtained in term of Bessel functions by suitably choosing coefficients so that the initial and boundary conditions are satisfied:

$$\varphi(r, t) = \sum_{n=1}^{\infty} A_n J_0(\alpha_n r) \exp(-D\alpha_n^2 t) \quad (14)$$

Thus, if the initial concentration distribution is φ_0 through the radius, and the surface $r = R$ is maintained at zero concentration, then we have:

$$J_0(R\alpha_n) = 0 \quad (15)$$

where $J_0(x)$ is the Bessel function of the first kind of order zero. The first one hundred roots of $J_0(x)$ are tabulated in Table 1 in the appendix.

The solution of Eq. (10) can be finally expressed as:

$$\varphi_C(r, t) = \varphi_0 \cdot \frac{2}{R} \sum_{n=1}^{\infty} \frac{J_0(r\alpha_n)}{\alpha_n J_1(R\alpha_n)} \exp(-D\alpha_n^2 t) \quad (16)$$

However, if there are no holes on regolith container side face, the diffusion process must be treated as one dimensional (linear) diffusion in depth direction. We also view LRS as homogeneous in all directions for gas diffusion, Eq. (9) can be simplified to:

$$\frac{\partial\varphi}{\partial t} = D \frac{\partial^2\varphi}{\partial z^2} \quad (17)$$

The boundary conditions can be given as:

$$\begin{cases} \varphi = \varphi_0 \text{ in } 0 < x < 2H \text{ when } t = 0 \\ \varphi = 0 \text{ in } x = 2H \text{ when } t > 0 \end{cases} \quad (18)$$

The solution for Eq. (17) can be obtained as:

$$\varphi_L(x, t) = \frac{4\varphi_0}{\pi} \sum_{n=0}^{\infty} \frac{1}{2n+1} \sin \frac{(2n+1)\pi x}{2H} \quad (19)$$

$$\times \exp \left(- \left(\frac{(2n+1)\pi}{2H} \right)^2 Dt \right) (n = 0, 1, 2 \dots) \quad (19)$$

What we care most is the pressure in the position with the longest diffusion path. In cylindrical (proposed) diffusion, the axis has the longest path of (radius) for gas diffusion, while in linear (conventional) diffusion, the regolith bottom has the longest diffusion path of (height), and H is 8 times of R . Given a constant gas diffusion coefficient of $D = 4 \times 10^{-5}$ (by assumption according to the experimental result in Fig. 6G), then the pressure variation with the longest diffusion path is presented in Fig. 7. The axis pressure decreases to the order of 10^{-1} Pa in cylindrical diffusion, while the bottom pressure only has an extremely small reduction in linear diffusion. It is obvious that the cylindrical method has a dramatically faster diffusion than that of the linear method, proving the efficiency of our methodology.

5.1.2. Heat transfer mechanism

In particulate and porous LRS, heat is mainly transferred by three paths: (i) solid conduction within regolith particles and across interparticle contacts, (ii) gas convection across interparticle void space, and (iii) radiation within regolith particles and interparticle void space [45]. In solids or liquids, heat is dominantly transferred through conduction, while the contribution of convection and radiation dominates heat transfer in LRS. Although the heat transfer coupling mechanism is extremely complex, the most conventional way is to assign a contribution of thermal conductivity to each mechanism in previous study [45]:

$$k_{eq} = k_{solid} + k_{gas} + k_{rad} \quad (20)$$

The term k_{gas} is often ignored when measuring the thermal conductivity of LRS in vacuum, and then k_{eq} is conventionally fitted as the Watson's Equation [20]:

$$k_{eq} = A + BT^3 \quad (21)$$

However, when we take insights into the relationship between thermal conductivity and pressure/temperature/porosity simultaneously, previous models do not work well in predicting the equivalent thermal conductivity. In our model, we add a conduction–convection coupling term, and the revised equivalent thermal conductivity is given as:

$$k_{eq} = k_{solid} + k_{gas} + k_{rad} + k_{sg} \quad (22)$$

At NAP, k_{gas} and k_{sg} dominate heat transfer, while they are ignored in vacuum because gas is pumped away. We expand Eq. (22) with variables of temperature, pressure, and porosity as:

$$k_{eq}(T, P, \phi) = g_{solid}(\phi) k_{basalt}(T) + g_{gas}(P, \phi) (k_{air}(T) + C_{sg} k_{basalt}(T)) + g_{rad}(\phi) \cdot T^3 \quad (23)$$

It is worth noting that we assume g_{solid} and g_{rad} only depend on porosity, and g_{gas} merely depends on pressure and porosity. The constant C_{sg} illustrates the coupling effect between solid conduction and gas convection. Eq. (23) is a generic presentation of thermal conductivity to all particulate and porous materials, like LRS, in moderate temperature, gas pressure and porosity. The porosity of LRS can be easily given by:

$$\phi = 1 - \frac{\rho}{\rho_{solid}} \quad (24)$$

The solid conduction term is basically modeled on the assumption that heat transfers between spherical regolith particles. Although LRS particles have irregular shape, this simplification is mainly for easy calculation. We assume LRS particles to spheres with equivalent radius R_p , which can be calculated according to its particle size distribution:

$$R_p = \frac{\sum_{i=1}^n \frac{m_i}{R_i^2}}{\sum_{i=1}^n \frac{m_i}{R_i^3}} \quad (25)$$

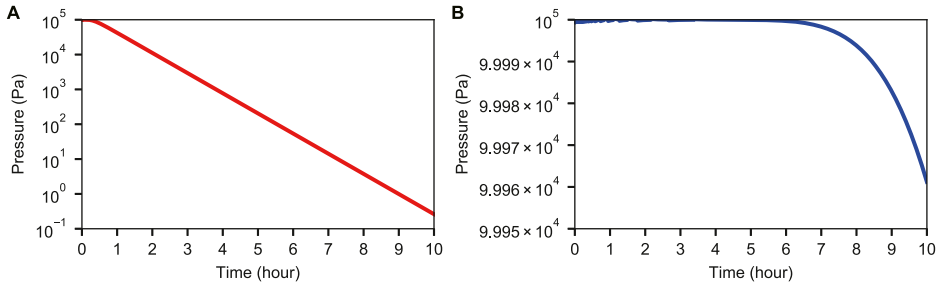


Fig. 7. Gas diffusion comparison through different paths. (A) Axis pressure ($R = 0.25$ m) versus time in cylindrical diffusion. (B) Bottom pressure ($H = 2.0$ m) versus time in linear diffusion.

where m_i and R_i are given by particle size distribution. Then we obtain the solid conduction relationship with that of basalt as [2,46]:

$$g_{solid}(\phi) = \frac{4}{\pi^2} (1 - \phi) \eta \xi \frac{r_c}{R_p} \quad (26)$$

where the coordination number η can be calculated as a function of porosity:

$$\eta = \frac{2.812(1 - \phi)^{-1/3}}{\Omega^2 (1 + \Omega^2)} \quad (27)$$

where $\Omega = 0.07318 + 2.193\phi - 3.357\phi^2 + 3.194\phi^3$. For ideal spheres without surface roughness, the radius of the contact area can be expressed by the JKR theory as [46]:

$$r_c = \left(\frac{3(1 - \nu^2)}{4E} \left(F_p + \frac{3}{2}\pi\kappa R_p + \sqrt{3\pi R_p F_p + \left(\frac{3}{2}\pi\kappa R_p \right)^2} \right) R_p \right)^{1/3} \quad (28)$$

For small volume of LRS for thermophysical test, we assume the force exerted to regolith particles F_p to be zero, then Eq. (28) can be simplified as:

$$r_c = \left(2.25 (1 - \nu^2) \pi \gamma R_p^2 / E \right)^{1/3} \quad (29)$$

For typical basalt rock, its thermal conductivity variation with temperature can be given by [46]:

$$k_{basalt}(T) = -9.53 \times 10^{-4} \cdot T + 2.40 \quad (30)$$

Gas is composed of a great number of particles behaving like spherical balls in a state of random and constant motion. Gas convection is due to the colliding energy exchange of gas molecules, while the solid–gas coupling term is generated because of colliding energy exchange between solid regolith particles and interparticle gas molecules. Previous model neglects this coupling term, nevertheless the model still works well for thermal conductivity prediction in vacuum. As pressure decreases, the colliding energy exchange deduces, resulting in lower gas convection and solid–gas coupling heat exchange. We construct g_{gas} basing on the method in Ref. [1] as follows:

$$g_{gas}(P, \phi) = \frac{1}{1 + f(\phi) \frac{300}{P}} \quad (31)$$

$$f(\phi) = C_{gas} \frac{\xi}{(1 + \xi)} \frac{(1 - \phi)}{\phi} \frac{1}{D_p \sigma^2 N_{Pr}} \quad (32)$$

Heat transfer inside regolith particles is more efficient than that in gas, which can be concluded from the thermal conductivities of basalt (2.40 W/(m K)) and air (0.026 W/(m K)) in room environment. For air in room condition, its thermal conductivity variation with temperature can be given by [47]:

$$k_{air}(T) = 7.69 \times 10^{-5} \cdot T - 3.18 \times 10^{-3} \quad (33)$$

The radiative conductivity can be modeled as the heat transfer through multi-layer medium, which is proportional to the temperature

T and the efficient distance L_r between the layers:

$$g_{rad} = \frac{4\epsilon}{2 - \epsilon} \sigma_{SB} L_r \quad (34)$$

$$L_r = 2C_{rad} \left(\frac{\phi}{1 - \phi} \right)^{1/3} R_p \quad (35)$$

Then, we build a comprehensive model to predict heat transfer of LRS with temperature, pressure and porosity.

5.2. Experimental comparison

5.2.1. Gas transfer mechanism

What we mostly concern about the thermal-vacuum simulation of LRS is the mechanism how heat and gas are transferred during the pump down process. With our proposed design, inner gas flows out of LRS in all directions during evacuation process (Fig. 8A), and the gas diffusion path is much shorter than that of conventional method (Fig. 8B). According to Fick's diffusion theory, larger path leads longer time to diffuse, which means even the chamber has reached desired vacuum, while the pressure inside LRS is still high. In the static pressurization experiment to evaluate the leaking and outgassing of the chamber, pressure gradually increased from 9×10^{-2} Pa to 100 Pa within 90 min after closing the pump system, and the total gassing load was almost constant at 73.94 Pa L/s in this process (Fig. 8C). However, the pressure inside LRS was much higher than the chamber pressure (Fig. 8D), even at the time the diffusion pump started, leading a sharp decrease in chamber pressure, while the influence on the pressure inside LRS was unobvious. Before calculating the outgassing rate of LRS, we obtained the nominal pump speed first (Fig. 8E), which has clear turning points when pump transferred. Based on vacuum theory, we obtained the outgassing rate of LRS during the pump down process, which is almost on the order of 10^{-1} Pa L/(s cm²) after 1 h (Fig. 8F). In Fig. 8G, we compared the outgassing rates of different materials, covering metal, rubber, plastic, lipid, fiber, and organic/inorganic material. The outgassing rates of conventional metals used for vacuum system with different processing technologies are in the range of $10^{-7} \sim 10^{-4}$ Pa L/(s cm²). For material with large outgassing rate, such as rubber, plastic, and fiber, the maximum outgassing rate is merely on the order of 10^{-3} Pa L/(s cm²). This value can be an effective index in measuring the evacuation difficulty and provides important reference to pump down LRS.

5.2.2. Heat transfer mechanism

To illustrate heat transfer mechanism inside particulate LRS, we think heat is transferred by four paths, including solid conduction, gas convection, radiation, and solid–gas coupling term (Fig. 9A). In vacuum, the terms related to gas convection can all be neglected, and solid conduction contributes mainly. We compared the theoretical value with the measured thermal conductivity of lunar sample when pressure varies. For pressure less than 0.1 torr (13.3 Pa), the modeling data fits the sample data pretty well, and thermal conductivity almost remains constant when pressure decreases (Fig. 9B). In the range of

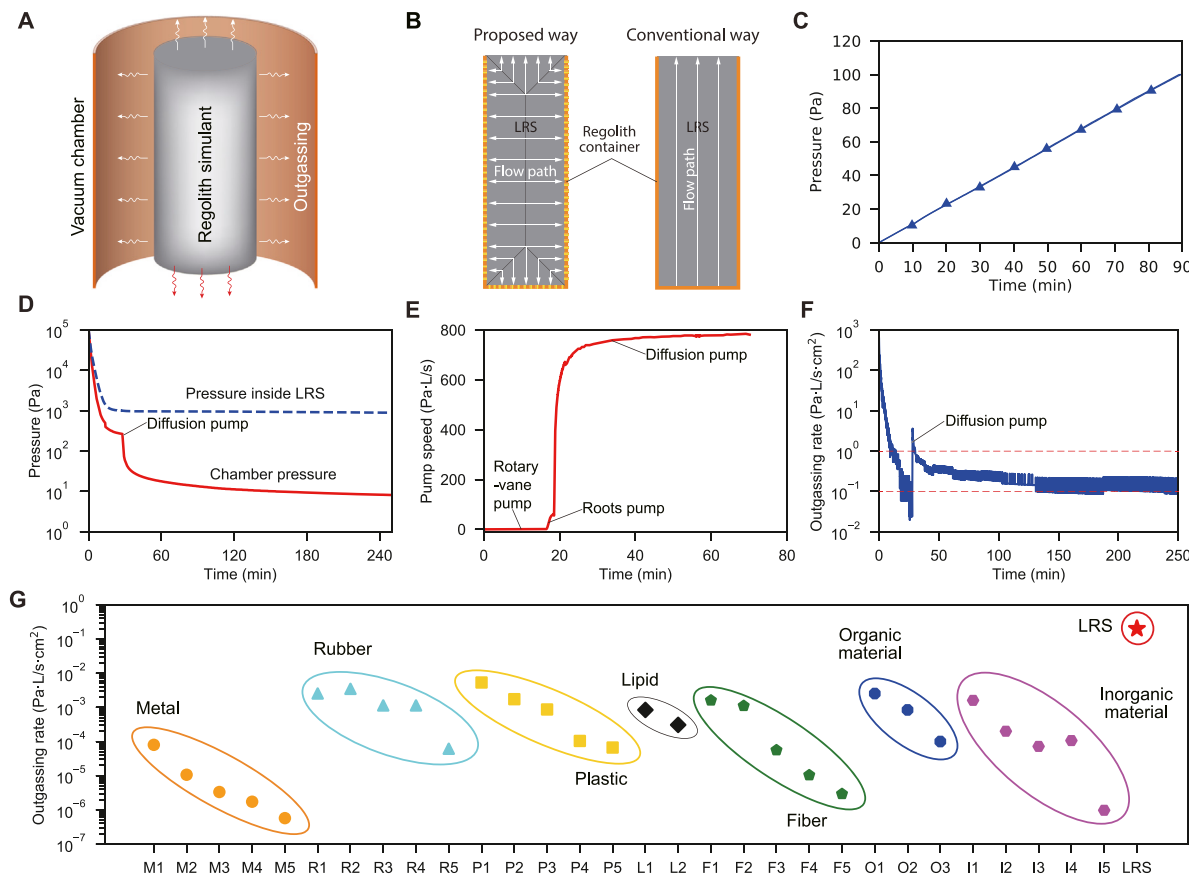


Fig. 8. Gas transfer mechanism in LRS. (A) Schematic illustration of outgassing of compacted LRS in vacuum. (B) Gas flow path comparison between proposed and conventional methods. The longest path in our method is along the container radius, while it is along the height in conventional method. (C) Static pressurization experiment reflected chamber leaking and outgassing. The chamber was pumped to 9×10^{-2} Pa, and then the pump system was closed. The chamber pressure increased gradually due to chamber leaking and outgassing. (D) Pressure inside LRS (blue line) and chamber pressure (red line) versus time. The pressure inside LRS was measured by the gauge fixed as Fig. 3F. (E) Nominal pumping speed versus time. (F) LRS's outgassing rate versus time. (G) One-hour outgassing rate of conventional materials, whose full names are presented in Table 2 in the appendix. (For interpretation of the references to colour in this figure legend, the reader is referred to the web version of this article.)

$10^1\text{--}10^3$ torr, the modeling value is some higher than sample data, but it still fits the thermal conductivity of the fabricated LRS well. The theoretical model predicts the thermal conductivities of lunar samples returned in Apollo 11/12 missions (Fig. 9C) and the fabricated LRS (Fig. 9D) well when temperature changes. In vacuum, thermal conductivity decreases as porosity increases for solid conduction is weakened and gas convection does not exist, while in room condition, thermal conductivity increases as the increase of porosity because gas convection is strengthened (Fig. 9E). For thermal gradient simulation, we set different thermal conductivities with the same boundary temperature of 228 K (Fig. 9F) and the same axis temperature of 183 K (Fig. 9G) to evaluate the refrigerating performance. The temperature nephogram after 24 h clearly demonstrates that in vacuum it is inefficient to refrigerate LRS in LRE simulation. One more efficient way is to reasonably distribute cold sources inside LRS, and to embed considerable temperature sensors to measure the entire thermal field.

6. Application in Chinese Chang'E 5 mission

As the final mission scheduled for the first three-stage of China's Chang'E lunar exploration program, Chang'E 5 mission plans to be executed at the end of 2020, aiming to penetrate at least 2 m into lunar regolith, sample subsurface lunar regolith, and return collected sample to Earth [48]. As a generic method to serve lunar exploration, the proposed methodology provides an excellent way for drilling and sampling test in simulated LRE. To further illustrate the potential application of the LRE simulating methodology, we designed and fabricated

a drilling test-bed aiming to penetrate two m as Chinese Chang'E 5 mission will do, including penetration, rotation and percussion, driven by three motors separately, and tested it with the same operational parameters (Fig. 10). To fulfill the testing authenticity and low cost meanwhile, the test-bed was designed to be mounted on the top of the vacuum chamber, while the drill tool was stretched into the chamber to complete sampling test in thermal-vacuum condition. The main purpose is to validate the drilling force and thermal performance of penetrating in simulated LRE. Drilling temperature and force were monitored by thermocouples and force sensors, respectively [30,49].

The results of the drilling test are presented in Fig. 11A to C. During the penetration, the chamber vacuum was maintained between 6~8 Pa, and the regolith temperature is depicted as Fig. 6F. It takes 16 min to reach a penetration depth of 2 m, with an average penetration rate of 125 mm/min and a rotational speed of 120 rpm. The maximum temperature on the drill bit cutter reached nearly 130 °C, and this temperature changed rapidly with penetration force. Temperature rising on the auger and core pipe is unobvious, only with an increment in the range of 10~15 °C. That means in such sampling condition, the influence caused by temperature will little change the composition of sampled regolith. This test could effectively estimate the influence of drilling temperature to drill bit and drilled samples.

7. Discussion

7.1. Methodology limitation

Although this work covers many aspects of the methodology to construct LRE, the focus is on LRS fabrication and thermal vacuum

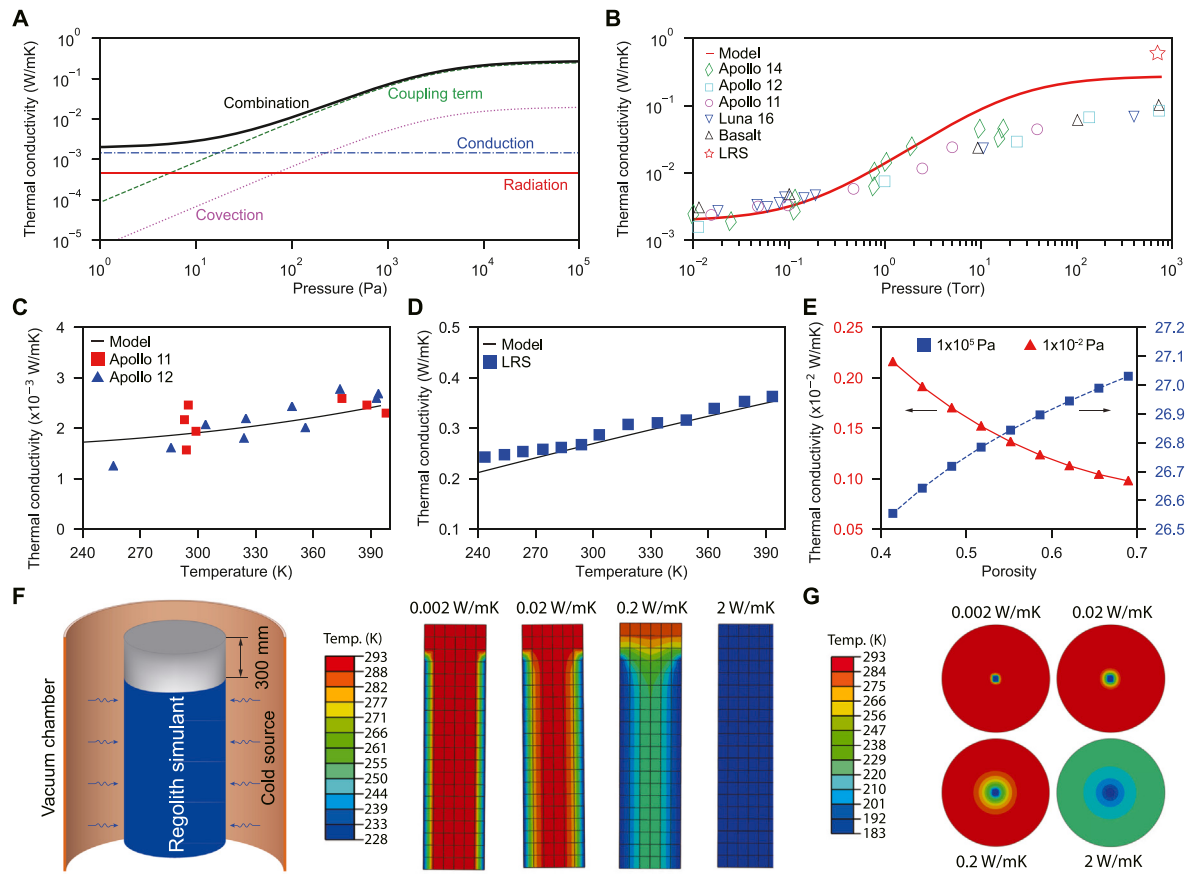


Fig. 9. Heat transfer mechanism in LRS. (A) Theoretical thermal conductivity versus pressure, including conductive, convective, radiative, and coupling terms. (B) Thermal conductivity comparison between model and sample (cited from Ref. [43]). (C) Theoretical thermal conductivity versus temperature in vacuum. The sample data is from Ref. [21,38]. (D) Theoretical thermal conductivity versus temperature at NAP. The sample data is from Fig. 2H. (E) Theoretical thermal conductivity versus porosity in vacuum (red line) and at NAP (blue line). (F) Refrigeration with constant surface temperature of 228 K in vacuum and temperature nephogram with different thermal conductivities after 24 h. (G) Temperature nephogram (axis refrigeration by a 30-mm copper tube with constant temperature of 183 K) with different thermal conductivities after 24 h, in which 0.002 W/(m·K) is close to that of lunar regolith in vacuum, 0.2 W/(m·K) is approximate to that of LRS in room condition, and 2 W/(m·K) is near to that of basalt rock. (For interpretation of the references to colour in this figure legend, the reader is referred to the web version of this article.)

realization. There are also some limitations that need to be improved for extensive application. We summarize these limitations as follows:

- (1) *Bulk density with depth*: According to the information acquired from previous lunar exploration missions, the bulk density of lunar regolith is not constant, with an increase from loose surface (1200 kg/m^3) to dense subsurface (2000 kg/m^3). Although the layer-by-layer compaction in our methodology is able to acquire different average bulk densities through controlling vibration time, we do not consider density variation with depth yet. For application scenarios that the bulk density increase must be strictly controlled, the usage of this method may be limited.
- (2) *Accurate thermal field control*: In vacuum condition, the heat transfer is greatly weakened, resulting in low thermal conductivity and then very slow heat exchange process. The larger the LRS size is, the longer it takes to establish a steady thermal field. On the scale of m, it is time-consuming to acquire the low temperature field of subsurface lunar regolith. Another problem is the inconsistency of thermal field, which is an inevitable issue in heat transfer process. How to lay cold source reasonably and how to control refrigerating rate accurately are extremely important to acquire desired regolith temperature field.
- (3) *Thermophysical equivalence*: The thermal conductivity of actual lunar regolith returned from American Apollo missions in vacuum is on the order of 10^{-3} W/(m K) . Whereas the measured thermal conductivity of our LRS is much larger, i.e. on the order of 10^{-2} W/(m K) . There are maybe two reasons for this: (i)

The thermal conductivity of actual lunar regolith samples were measured on the order of 10^{-4} Pa , which is much higher than the 1-Pa vacuum in our measurement. Though previous researches show that thermal conductivity is less affected by gas pressure below 10 Pa, the influence still exists. (ii) The second is the difference between actual lunar regolith and LRS. Lunar regolith particle is porous due to extremely long time erosion by space environment, which is impossible to achieve for LRS particle. Larger porosity leads to smaller thermal conductivity as heat transfer through solid conduction is highly reduced.

- (4) *Ingredient equivalence*: The raw material for LRS manufacture was collected from terrestrial volcano scoria. Though its chemical and mineral ingredients are similar to that of actual lunar regolith, it also contains many other ingredients do not exist in lunar regolith, such as microbe and organism. The proposed methodology focuses on thermal vacuum condition establishment and ignores some other factors. It is obvious that this technique is inappropriate, or at least needs to be improved, for possible biological research in lunar regolith. We hope to continuously improve this method to make it more widely applicable.

7.2. Application prospect

Developing the environmental conditions of planetary regolith for laboratory experiments is a prerequisite for the design and space qual-

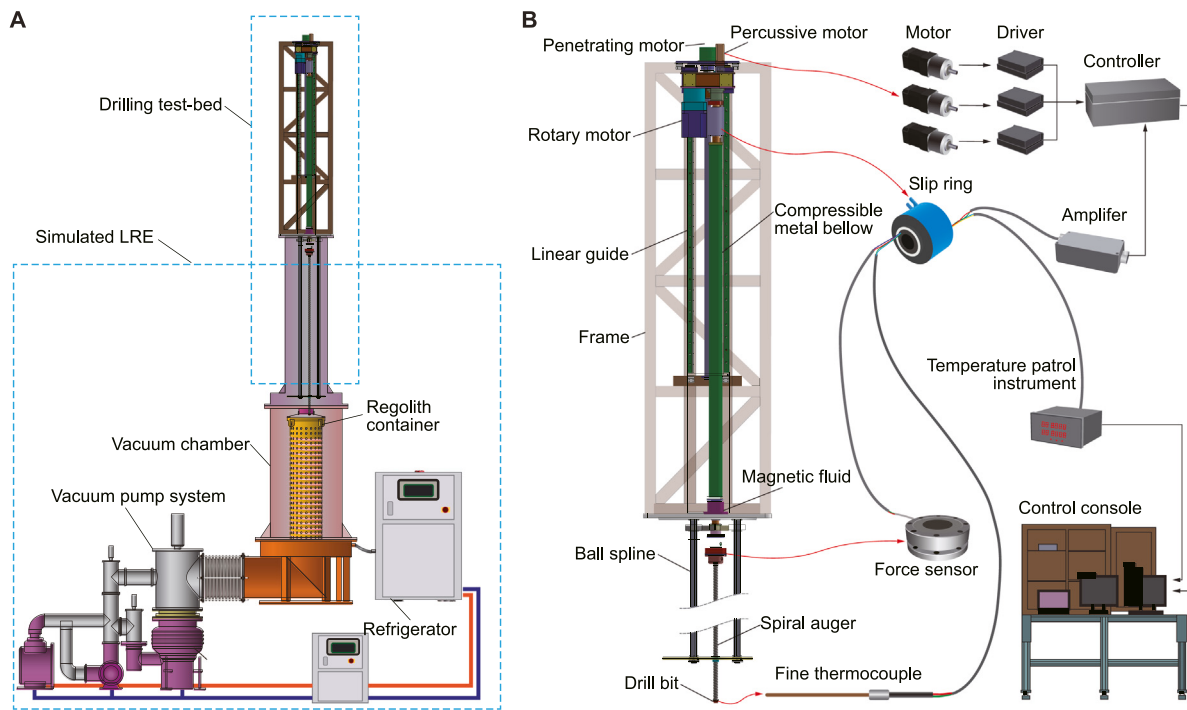


Fig. 10. Experimental setup for testing the drilling sampler for Chinese Chang'E 5 mission. (A) Schematic illustration of the testing strategy. The movement between the drill tool and the vacuum chamber is sealed by the combination of magnetic fluid and compressible metal bellow. (B) Schematic illustration of the drilling test-bed. Drilling temperature distribution on the drill tool was measured by fine thermocouples with a diameter of 0.5 mm. A force sensor measured penetration force and rotational torque. Signals were transferred through vacuum feedthroughs for chamber sealing, and a slip ring to avoid cable winding.

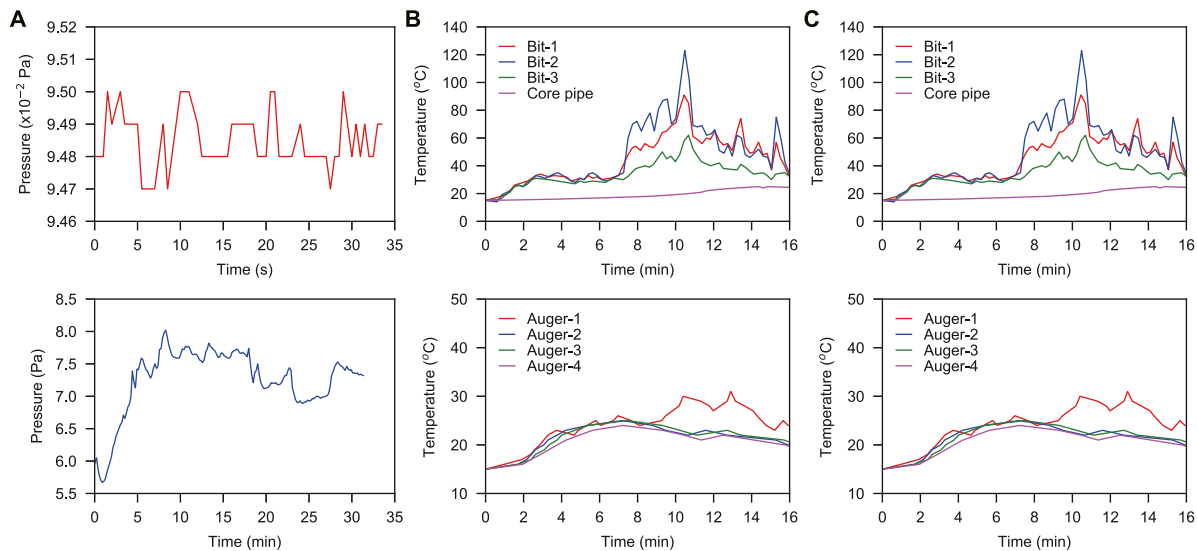


Fig. 11. Experimental results. (A) Chamber pressure variation when the drilling test-bed moved without LRS (top) and with LRS (bottom). When LRS was not included, the test was mainly to validate the dynamical sealing performance of the proposed method. (B) Drilling load versus time in penetrating LRS to 2 m: penetration force (top) and rotational torque (bottom). (C) Drill tool temperature versus time: bit temperature (top) and auger temperature (bottom). The location of each sensor was presented in our previous publications [30,50].

fication of any payload intend to planetary surface/subsurface probing by *in-situ* techniques. One can envisage the robotic army on extraterrestrial celestial bodies carrying out many tasks, including scientific experiments, for their masters on Earth, in the near future. To reach this level, we need to conduct many experiments on our laboratories before the landers landing on planet surface. Here, we give a brief application prospect of our methodology for future planetary exploration.

(1) *Lunar highland regolith environment construction:* According to the *in-situ* measurement of lunar regolith at different landing sites and the results of terrestrial observation and analysis, lunar regolith has an average thickness of 3~5 m. However, the ingredient and property of lunar regolith varies greatly with sites. Lunar highland terrain is more ancient than lunar mare terrain, which is exposed to the lunar surface for a longer period of time. The proposed method could be expanded to construct the

thermal vacuum environments in lunar highland terrain on condition that the regolith information on the exact site is known, such as chemical and mineral ingredients, and mechanical and thermophysical properties.

- (2) *Lunar polar regolith environment construction:* With the progress of lunar exploration and water ice was confirmed in lunar polar region, more and more attention is paid on this special place in recent years. By substituting dry LRS with irrigated LRS in the proposed methodology, we think this method can be applied to construct lunar polar regolith environment. If LRS is irrigated with water, then water changes into ice during refrigeration. It is much easier to pump freezing LRS than dry and waterless LRS because water fills inter-particle and inner-particle space. Less gas remains inside LRS, therefore a high vacuum is easier to be reached from the viewpoint of gas diffusion.
- (3) *Martian regolith environment construction:* Unlike dry and airless lunar regolith, Martian regolith contains water and gas, and Martian surface temperature diurnal variation is not that severe because of the existence of atmosphere. Compared with lunar regolith, the geological and chemical ingredients, and mechanical and thermophysical properties of Martian regolith is much different. This work can also provide a reference for Martian regolith environment construction with Martian regolith simulant in proper Martian environmental parameters. It is foreseeable that Martian regolith environment construction may be easier for relative lower vacuum (600 Pa) and stronger heat transfer capability (water existence in regolith).

8. Conclusion

Taking inspiration from tofu making procedure, this work presents a comprehensive methodology for LRE construction. The outgassing rate of LRS provides reference for LRE simulation and makes the vacuum realization of LRS calculable. Convection and conduction coupling mechanism demonstrates the feasibility to estimate the heat transfer of LRS under any pressure and temperature. Engineering demonstration of penetration in LRE produced by the methodology indicates the possibility of its future applications in planetary exploration technologies.

Declaration of competing interest

The authors declare that they have no known competing financial interests or personal relationships that could have appeared to influence the work reported in this paper.

Acknowledgments

Beihang University and Guangdong University of Technology contributed equally in this work. T.Z. thanks Z.L. for her helpful suggestions to improve the readability of this manuscript, for her help in making traditional Chinese tofu, and for her time to look after their new born baby, which greatly helps him to concentrate on preparing this work. T.Z. also thanks for S.Y. and J.L. for their help in designing the experiment testbed, and S.T. for his help in conducting the experiments. Funding: The work is financially supported in part by the NSFC, China Key Project (Grant No. 91748201), the NSFC, China Normal Project (Grant No. 51775011), the NSFC, China project for Young Scientists (Grant No. 51905105), the regular project of Natural Science Foundation of Guangdong Province, China (Grant No. 2020A151501505), the State Key Laboratory of Robotics and Systems (HIT), China (Grant No. SKLRS-2020-KF-12), the Seed Fund of Guangdong University of Technology, China, and the project of China Academy of Space Technology.

Appendix A. Supplementary data

Supplementary material related to this article can be found online at <https://doi.org/10.1016/j.actaastro.2020.08.039>.

References

- [1] W. Schotte, Thermal conductivity of packed beds, *AIChE J.* 6 (1) (1960) 63–67.
- [2] N. Sakatani, K. Ogawa, M. Arakawa, S. Tanaka, Thermal conductivity of lunar regolith simulants JSC-1A under vacuum, *Icarus* 309 (2018) 13–24.
- [3] Y. Bar-Cohen, K. Zacny, *Drilling in Extreme Environments: Penetration and Sampling on Earth and other Planets*, first ed., John Wiley and Sons, Hoboken, New Jersey, 2009.
- [4] Y. Gao, S. Chien, Review on space robotics: Toward top-level science through space exploration, *Sci. Robot.* 2 (7) (2017) eaan5074.
- [5] D.F. Lester, K.V. Hodges, R.C. Anderson, Exploration telepresence: A strategy for optimizing scientific research at remote space destinations, *Sci. Robot.* 2 (7) (2017) eaan4383.
- [6] T. Zhang, K. Xu, Z. Yao, X. Ding, Z. Zhao, X. Hou, Y. Pang, X. Lai, W. Zhang, S. Liu, J. Deng, The progress of extraterrestrial regolith-sampling robots, *Nat. Astronom.* 3 (6) (2019) 487–497.
- [7] C. Li, C. Wang, Y. Wei, Y. Lin, China's present and future lunar exploration program, *Science* 365 (6450) (2019) 238–239.
- [8] V. Stamenković, L. Beegle, K. Zacny, D. Arumugam, P. Baglioni, N. Barba, J. Baross, M. Bell, R. Bhartia, J. Blank, The next frontier for planetary and human exploration, *Nat. Astronom.* (2019) 116–120.
- [9] Y.G. Shkuratov, N.V. Bondarenko, Regolith layer thickness mapping of the moon by radar and optical data, *Icarus* 149 (2) (2001) 329–338.
- [10] X. Hou, T. Ding, T. Chen, Y. Liu, M. Li, Z. Deng, Constitutive properties of irregularly shaped lunar soil simulant particles, *Powder Technol.* (2019) 137–149.
- [11] C.S. Cockell, S. McMahon, Lifeless martian samples and their significance, *Nat. Astronom.* 3 (6) (2019) 468–470.
- [12] V. Badescu, *Moon: Prospective Energy and Material Resources*, Springer Science & Business Media, 2012.
- [13] S. Chien, K.L. Wagstaff, Robotic space exploration agents, *Sci. Robot.* 2 (7) (2017) eaan4831.
- [14] K. Zacny, G. Paulsen, M. Szczesiak, J. Craft, P. Chu, C. McKay, B. Glass, A. Davila, M. Marinova, W. Pollard, Lunarpvader: Development and testing of lunar drill in vacuum chamber and in lunar analog site of antarctica, *J. Aerosp. Eng.* 26 (1) (2012) 74–86.
- [15] J. Kleinhenz, A. Wilkinson, Isru soil mechanics vacuum facility: Soil bin preparation and simulant strength characterization, in: 50th Aerospace Sciences Meeting and Exhibit, AIAA, Nashville, Tennessee, United States, 2012, pp. 1–8.
- [16] G. Heiken, D. Vaniman, B.M. French, *Lunar Sourcebook: A User's Guide to the Moon*, CUP Archive, Cambridge, UK, 1991.
- [17] A.R. Vasavada, J.L. Bandfield, B.T. Greenhagen, P.O. Hayne, M.A. Siegler, J. Williams, D.A. Paige, Lunar equatorial surface temperatures and regolith properties from the diviner lunar radiometer experiment, *J. Geophys. Res.: Planets* (1991–2012) 117 (E12) (2012) E00H18.
- [18] A.R. Vasavada, D.A. Paige, S.E. Wood, Near-surface temperatures on mercury and the moon and the stability of polar ice deposits, *Icarus* 141 (2) (1999) 179–193.
- [19] V. Gromov, Physical and mechanical properties of lunar soil, *Earth, Moon, Planets* (80) (1999) 51–72.
- [20] R. Woods Robinson, M.A. Siegler, D.A. Paige, A model for the thermophysical properties of lunar regolith at low temperatures, *J. Geophys. Res.: Planets* 124 (7) (2019) 1989–2011.
- [21] C. Cremers, R. Birkebak, Thermal conductivity of fines from apollo 12, in: 2nd Lunar Science Conference, MIT Press, Houston, Texas, United States, 1971, pp. 2311–2315.
- [22] B. Hemingway, R. Robie, W. Wilson, Specific heats of lunar soils, basalt, and breccias from the apollo 14, 15, and 16 landing sites, between 90 and 350 k, in: 4th Lunar and Planetary Science Conference, Lunar and Planetary Institute, Houston, Texas, United States, 1973, pp. 2481–2487.
- [23] T. Zhang, X. Ding, K. Xu, S. Liu, L. He, H. Zhu, Y. Guan, Evacuation method and outgassing rate of a lunar regolith simulant for deep drilling tests, *Acta Astronaut.* 157 (2019) 455–464.
- [24] K. Zacny, J. Craft, A. Davila, G. Paulsen, C. McKay, M. Marinova, B. Mellerowicz, B. Glass, W. Pollard, Lunarpvader: Testing of a 1 m lunar drill in a 3.5 m vacuum chamber and in the antarctic lunar analog site, in: IEEE Aerospace Conference, IEEE, Big Sky, Montana, United States, 2012, pp. 1–9.
- [25] R.W. Carlson, Analysis of lunar samples: Implications for planet formation and evolution, *Science* 365 (6450) (2019) 240–243.
- [26] T. Szwarc, A. Aggarwal, S. Hubbard, B. Cantwell, K. Zacny, A thermal model for analysis and control of drilling in icy formations on mars, *Planet. Space Sci.* 73 (1) (2012) 214–220.
- [27] J. Cui, X. Hou, Z. Deng, W. Pan, Q. Quan, Prediction of the temperature of a drill in drilling lunar rock simulant in a vacuum, *Therm. Sci.* 21 (2) (2017) 989–1002.

- [28] H. Kanamori, S. Udagawa, T. Yoshida, S. Matsumoto, K. Takagi, Properties of lunar soil simulant manufactured in Japan, in: Space, Vol. 98, 1998, pp. 462–468.
- [29] X. Xu, S. Xiao, T.B. Rahardjo, E. Hogervorst, Tofu intake is associated with poor cognitive performance among community-dwelling elderly in China, *J. Alzheimer's Dis.* 43 (2) (2015) 669–675.
- [30] T. Zhang, X. Ding, S. Liu, K. Xu, Y. Guan, Experimental technique for the measurement of temperature generated in deep lunar regolith drilling, *Int. J. Heat Mass Transfer* 129 (2) (2019) 671–680.
- [31] K.-i. Horai, G. Simmons, H. Kanamori, D. Wones, Thermal diffusivity, conductivity and thermal inertia of apollo 11 lunar material, *Geochim. Cosmochim. Acta Suppl. 1* (1970) 2243–2249.
- [32] C. Cremers, H. Hsia, Thermal conductivity and diffusivity of apollo 15 fines at low density, in: Lunar and Planetary Science Conference Proceedings, Lunar and Planetary Institute, Houston, Texas, United States, 1973, pp. 2459–2464.
- [33] C. Cremers, H. Hsia, Thermal conductivity of apollo 16 lunar fines, in: Lunar and Planetary Science Conference Proceedings, Lunar and Planetary Institute, Houston, Texas, United States, 1974, pp. 2703–2708.
- [34] J. Mitchell, W. Houston, R. Scott, N. Costes, W. Carrier III, L. Bromwell, Mechanical properties of lunar soil: Density, porosity, cohesion and angle of internal friction, in: 3rd Lunar and Planetary Science Conference, MIT Press, Cambridge, Massachusetts, United States, 1972, pp. 3235–3253.
- [35] J. Graf, U.S.N. Aeronautics, S.A. Scientific, T.I. Program, Lunar Soils Grain Size Catalog, NASA, Office of Management, Scientific and Technical Information Program, 1993.
- [36] J. Papike, S.B. Simon, J. Laul, The lunar regolith: Chemistry, mineralogy, and petrology, *Rev. Geophys.* 20 (4) (1982) 761–826.
- [37] D.S. McKay, J.L. Carter, W.W. Boles, C.C. Allen, J.H. Allton, Jsc-1: A new lunar soil simulant, in: R.G. Galloway, S. Lokaj (Eds.), Engineering, Construction, and Operations in Space IV, American Society of Civil Engineers, Albuquerque, New Mexico, United States, 1974, pp. 857–866.
- [38] C. Cremers, R. Birkebak, Thermal conductivity of fines from apollo 11, in: Apollo 11 Lunar Science Conference, Lunar and Planetary Institute, Houston, Texas, United States, 1970, pp. 2045–2050.
- [39] R.A. Robie, B.S. Hemingway, W.H.S. Wilson, Specific heats of lunar surface materials from 90 to 350 degrees kelvin, *Science* 167 (3918) (1970) 749–750.
- [40] B. Glass, H. Cannon, M. Branson, S. Hanagud, G. Paulsen, Dame: planetary-prototype drilling automation, *Astrobiology* 8 (3) (2008) 653–664.
- [41] J.E. Kleinhenz, R.A. Wilkinson, Development and Testing of an ISRU Soil Mechanics Vacuum Test Facility, Report, NASA, 2014.
- [42] A.E. Wechsler, P.E. Glaser, Pressure effects on postulated lunar materials, *Icarus* 4 (4) (1965) 335–352.
- [43] C. Tien, A. Nayak, Analytical models for lunar soil thermal conductivity, in: AIAA Tenth Thermophysics Conference, AIAA, Denver, Colorado, United States, 1975, pp. 1–8.
- [44] I. Bello, Vacuum and Ultravacuum: Physics and Technology, CRC Press, 2017.
- [45] A.E. Wechsler, P.E. Glaser, J.A. Fountain, Thermal properties of granulated materials, *Progr. Astronaut. Aeronaut.* 28 (1972) 215–241.
- [46] N. Sakatani, K. Ogawa, Y.-i. Iijima, M. Arakawa, R. Honda, S. Tanaka, Thermal conductivity model for powdered materials under vacuum based on experimental studies, *AIP Adv.* 7 (1) (2017) 015310.
- [47] J.P. Holman, Heat Transfer, Vol. 10, China Machine Press, Beijing, 2011.
- [48] Y. Wei, Z. Yao, W. Wan, China's roadmap for planetary exploration, *Nat. Astronom.* 2 (5) (2018) 346–348.
- [49] T. Zhang, Z. Zhao, S. Liu, J. Li, X. Ding, S. Yin, G. Wang, X. Lai, Design and experimental performance verification of a thermal property test-bed for lunar drilling exploration, *Chin. J. Aeronaut.* 29 (5) (2016) 1455–1468.
- [50] T. Zhang, X. Ding, A thermal model for predicting the drilling temperature in deep lunar regolith exploration, *Appl. Therm. Eng.* 128 (2018) 911–925.



CHAO Chaoyue received his B.Eng. degree from the School of Mechatronics and Vehicle Engineering, East China Jiaotong University, Nanchang, China, in 2019. He is currently pursuing his Master degree in the School of Electromechanical Engineering, Guangdong University of Technology, Guangzhou, China. His research interests include planetary and seafloor drilling robot.



YAO Zhixiao received his B.Eng. degree from the School of Mechanical and Power Engineering, Harbin University of Science and Technology, Harbin, China, in 2017. He is currently pursuing his Mater degree from the School of Electromechanical Engineering, Guangdong University of Technology, Guangzhou, China. His research interests include the research and development of a seafloor regolith-sampling robot and Martian regolith-sampling robot.



XU Kun received the B.Eng., M.Eng. and Ph.D. degrees in mechanical engineering from the School of Mechanical Engineering and Automation, Beihang University (Beijing University of Aeronautics and Astronautics, BUAA), Beijing, China, in 2005, 2008 and 2012, respectively. He is currently an associate professor in Robotics Institute at Beihang University. His research interests include robotics, mechanism theory, multi-legged robot, gait planning etc.



ZHANG Wuxiang received the M.Eng. degree in Non-Destructive Testing from Huazhong University of Science and Technology in 2004 and Ph.D. degree in Mechatronics Engineering from Beihang University (Beijing University of Aeronautics and Astronautics, BUAA) in 2010. He is currently an associate professor in Robotics Institute at Beihang University. His research interests include mechanisms, robotics, measurement technique, intelligent automatic device, testing technique, etc.



DING Xilun received the B.Eng. degree in mechanical engineering from Zhengzhou Institute of Technology, Zhengzhou, China, in 1991, and the M.Eng. degree in mechanical design and Ph.D. degree in mechatronics and automation from Harbin Institute of Technology, Harbin, China, in 1994 and 1997, respectively. From 1997~1998, he was a Postdoctoral Research Fellow at the Robotics Institute, Beihang University (Beijing University of Aeronautics and Astronautics, BUAA), Beijing, China, where he became an Associate Professor in 1998, and has been a Professor since 2004. From September 1999 to January 2000, he was a Senior Visiting Scholar at the Academy of Mathematics and Systems Sciences, Chinese Academy of Sciences. During September 2000 to September 2001, he was a Postdoctoral Research Fellow in the School of Computing, Information Systems and Mathematics, South Bank University, London, U.K. From 2006~2009, he was a Visiting Professor in Mechanical Engineering at King's College, London. His research interests include the dynamics of compliant mechanical systems and robots, nonholonomic control of pace robots, dynamics and control of aerial robots, and biomimetic robots. Dr. Ding was a recipient of the National Science Fund for Distinguished Young Scholars of China in 2011.



LIU Shuting received her B.Eng and M.Eng. degrees from the School of Mechanical Engineering and Automation, Beihang University (Beijing University of Aeronautics and Astronautics, BUAA), Beijing, China, in 2013 and 2015, respectively. Currently, she is a engineer in Beijing Institute of Space Long March Vehicle, China Academy of Launch Vehicle Technology, Beijing, China. Her research interests mainly include planetary mechanism, thermal vacuum environment simulation, structure design and optimization, etc.



ZHANG Tao received his B.Eng. and Ph.D. degrees from the School of Mechanical Engineering and Automation, Beihang University (Beijing University of Aeronautics and Astronautics, BUAA), Beijing, China, in 2012 and 2017, respectively. In 2017, he joined the Biomimetic and Intelligent Robotics Laboratory (BIRL), in the School of Electro-mechanical Engineering, Guangdong University of Technology, Guangzhou, China, as an assistant professor. His interests include planetary robot, extraterrestrial regolith environment construction, extraterrestrial and seafloor regolith-sampling robot, mechanism and machine theory, and bio-inspired robot. He became a member of IEEE and CMES since 2019.



ZHAO Zen received his B.Eng. degree from the School of Mechanical Engineering, North University of China, Taiyuan, China, in 2008, and Master degree from the School of Mechanical Engineering, University of Science and Technology Beijing, Beijing, China, in 2011. At the same year, he joined Beijing Spacecrafts as an engineer. He participated in the design and development of the lunar drilling and sampling system these years. He is currently a senior engineer and his research interests include mechanism design, mechatronic system, extraterrestrial regolith-sampling robot, etc.



AN Yinghe received his B.Eng and M.Eng. degrees from the School of Mechanical Engineering and Automation, Beihang University (Beijing University of Aeronautics and Astronautics, BUAA), Beijing, China, in 2010 and 2013, respectively. Currently, he is a senior engineer in Space Engineering Development Co., Ltd., China Aerospace Science and Industry Corporation, Beijing, China. His research interests mainly include drilling robot, planetary mechanism, thermal vacuum environment simulation, structure design and optimization, etc.



WANG Bing received his B.Eng. degree in Mechanical Design, Manufacturing and Automation from the School of Mechanical Engineering, University of Jinan in 2019. At present, he is a master student in the Biomimetic and Intelligent Robotics Laboratory (BIRL), School of Electro-mechanical Engineering, Guangdong University of Technology, Guangzhou, China. His research interests mainly include industrial robot, structure design, motion control, etc.



YU Shuangfei received his B.Eng. degree in aircraft manufacturing engineering from Nanchang Aeronautical University, Nanchang, China, in 2013. He worked in China Railway Rolling Stock Corporation (CRRC), Zhuzhou, China, as a chief engineer from 2013 to 2016. He received his M.Eng. degree from the School of Mechanical and Electrical Engineering in Wuyi university, Jiangmen, China, in 2019. Currently, he is a Ph.D. candidate in the Biomimetic and Intelligent Robotics Laboratory (BIRL), School of Electro-mechanical Engineering, Guangdong University of Technology, Guangzhou, China. His main research interests include intelligent manufacturing, robot vision, etc.



WANG Bin received his B.Eng. degree in Mechanical and Electronic Engineering from the School of Mechanical Engineering, Hunan Institute of Science and Technology, Yueyang, China, in 2019. Currently, he is a master student in the Biomimetic and Intelligent Robotics Laboratory (BIRL), School of Electro-mechanical Engineering, Guangdong University of Technology, Guangzhou, China. His research interests mainly include biomimetic manipulator, master-slave control, etc.



CHEN Haowen received his B.Eng. degree in Mechanical and Electronic Engineering from the School of Mechanical and Electrical Engineering, Guangdong University of Technology, Guangzhou, China, in 2018. Currently, he is a master student in the Biomimetic and Intelligent Robotics Laboratory (BIRL) in the same university. His research interests mainly include force control, robotic polishing, intelligent manufacturing, etc.